



Evidence of cloud sensitivity to above-cloud CCN as a function of environmental stability in the Southeast Atlantic based on remote sensing observations

Emily D. Lenhardt¹, Lan Gao¹, Siddhant Gupta², Greg M. McFarquhar^{1,3}, Feng Xu¹, Richard A. Ferrare⁴,
5 Chris A. Hostetler⁴, Jens Redemann¹

¹School of Meteorology, University of Oklahoma, Norman, OK, 73072, United States

²Environmental Science Division, Argonne National Laboratory, Lemont, IL, 60439

³Cooperative Institute for Severe and High-Impact Weather Research and Operations, University of Oklahoma, Norman, OK, 73072, United States

10 ⁴NASA Langley Research Center, Hampton, VA, 23681, United States

Correspondence to: Emily D. Lenhardt (emily.lenhardt@ou.edu)

Abstract. Information about the vertical distribution of cloud condensation nuclei (CCN) concentrations (N_{CCN}) is necessary for accurately quantifying aerosol-cloud interactions (ACI), as is constraining environmental conditions to separate aerosol effects from meteorological influences on clouds. Motivated by previous findings from the Southeast Atlantic, we investigate
15 ACI and their dependence on lower tropospheric stability (LTS) using a remote sensing-based data set. Utilizing a new machine learning (ML) method for retrieving N_{CCN} from High Spectral Resolution Lidar 2 (HSRL-2) observables, we assess the simultaneous impact of above- and below-cloud N_{CCN} on cloud microphysical properties via clear-sky, cloud-adjacent lidar profiles and collocated polarimetric retrievals of cloud properties. We observe a decrease in cloud droplet effective radius (R_{eff}) and an increase in cloud droplet number concentration (N_d), associated with an increase in above-cloud N_{CCN} .
20 Additionally, we find that the magnitude of these ACI are strongly dependent on LTS. We calculate $ACI_{REFE} = -\partial \ln(R_{eff}) / \partial \ln(N_{CCN})$ and $ACI_{CDNC} = d \ln(N_d) / d \ln(N_{CCN})$ and find that ACI_{REFE} decreases from 0.161 to 0.042 (-73.9 %) and ACI_{CDNC} decreases from 0.452 to 0.116 (-74.3 %) as LTS increases from 10 to 22 K. Additionally, we find that the relationship between below-cloud N_{CCN} and cloud top properties is weak and that above-cloud N_{CCN} – cloud property relationships are similar for cloud edge and cloud center observations. These findings demonstrate the importance of vertically resolved N_{CCN}
25 and consideration of LTS in ACI studies and establish a remote sensing-based analysis method with which future satellite studies can investigate ACI.

1 Introduction

Amidst several identified climate forcings that have and will continue to determine current and future climate warming, the highest uncertainty remains linked to aerosol-cloud interactions (ACI; Forster et al., 2021). Clouds play a significant role in
30 the climate system by regulating the atmosphere's radiative budget and surface precipitation, and they form when water vapor



condenses onto atmospheric aerosols that serve as cloud condensation nuclei (CCN) or ice nucleating particles. To improve the accuracy of climate model projections, the impact of such aerosols on cloud properties must be better understood and quantified (Seinfeld et al., 2016). Recent improvements in our understanding of cloud processes have suggested that in a warming climate, clouds may act to amplify warming instead of suppressing it (Forster et al., 2021). The strong dependence of our future climate on clouds and aerosols motivates continued efforts to reduce uncertainty associated with their interactions.

Increases in CCN concentration (N_{CCN}) at a fixed cloud liquid water path (LWP) are generally understood to reduce cloud droplet effective radius (R_{eff}) while increasing cloud droplet number concentration (N_d), thereby increasing the reflectance of clouds (Twomey, 1974). The nucleation of more numerous small droplets may delay or suppress the formation of raindrops by reducing collision-coalescence rates, thereby extending cloud lifetime (Albrecht, 1989) due to precipitation suppression and susceptibility to aerosols (e.g., Gupta et al., 2022a). Delayed precipitation formation can allow the cloud layer to reach higher cloud top heights (Andreae et al., 2004; Rosenfeld, 2006; Myhre et al., 2007), and the consequent increase in cloud geometric thickness can buffer the initial precipitation suppression via an increase in LWP. The numerous pathways and outcomes of ACI are interlinked, complicating our understanding of their overall effect on Earth's radiative budget because of the uncertainty associated with the sign and magnitude of their effective radiative forcing (Myhre et al., 2007; Forster et al., 2021). Additionally, local meteorology strongly governs cloud properties, making it difficult to disentangle aerosol effects from the effects of dynamics and meteorological regimes (McFarquhar et al., 2004; Lohmann et al., 2006; Mauger and Norris, 2007; Stevens and Feingold, 2009; Gryspeerdt et al., 2014; Rosenfeld et al., 2014; Zhang et al., 2016; Malavelle et al., 2017; Douglas and L'Ecuyer, 2019). Previous studies have constrained the impact of meteorology by developing regime-based approaches to constrain ACI as a function of cloud top pressure, cloud optical depth, vertical pressure velocity, lower tropospheric stability (LTS), estimated inversion strength (EIS), precipitation rate, and updraft velocity (Wood and Bretherton, 2006; Gryspeerdt and Stier, 2012; Gryspeerdt et al., 2014; Zhang et al., 2016; Chen et al., 2018; Zhao et al., 2025).

Many studies investigate evidence of ACI using retrievals of cloud microphysical properties from passive satellite instruments such as the Moderate Resolution Imaging Spectroradiometer (MODIS; Myhre et al., 2007; Alam et al., 2010; Goren and Rosenfeld, 2012; Chen et al., 2015; McCoy et al., 2017; Pan et al., 2018; Painemal et al., 2020; Gryspeerdt et al., 2022; Gupta et al., 2022b) and the Spinning Enhanced Visible and Infrared Imager (SEVIRI; Goren and Rosenfeld, 2012; Alexandri et al., 2024) or from active sensors such as CloudSat (Pan et al., 2018; Douglas and L'Ecuyer, 2019). Cloud retrievals from these platforms have been tested and evaluated against airborne in situ observations (Roebeling et al., 2008; Painemal and Zuidema, 2011; Min et al., 2012; King et al., 2013; Gupta et al., 2022b; Wang et al., 2024; Painemal et al., 2025). However, their aerosol observations are limited to columnar products such as aerosol optical depth (AOD), which may serve as an adequate N_{CCN} proxy over large spatiotemporal extents (Stier, 2016) but cannot fully explain N_{CCN} variance and lacks any information about the vertical distribution of N_{CCN} (Andreae, 2009; Shinozuka et al., 2015; Stier, 2016; Choudhury and Tesche, 2022a; 2022b). Additionally, aerosol retrievals from passive remote sensing platforms are limited to clear-sky conditions and are further limited spatially by cloud contamination and near-cloud aerosol humidification effects, meaning that their aerosol



65 products are often limited to those 15 km away from cloud edge (Christensen et al., 2017). These limitations often make passive aerosol retrievals insufficient for studying ACI.

The vertical distribution of N_{CCN} is especially relevant for ACI since N_{CCN} is of greater interest near the cloud base, where most cloud droplets nucleate. Therefore, many satellite-based studies have incorporated observations from the satellite-based Cloud-Aerosol Lidar with Orthogonal Polarization (CALIOP) to add information about aerosol vertical distributions (Várnai and Marshak, 2012; Costantino and Bréon, 2013; Pan et al., 2018; Douglas and L'Ecuyer, 2019; Painemal et al., 2020; 70 Li et al., 2025). However, collocation delays between different satellite platforms can cause data interpretation errors (Várnai and Marshak, 2012) and CALIOP measurements cannot provide information about below-cloud N_{CCN} distributions. Other studies have investigated ACI using ground-based (e.g., Lihavainen et al., 2010; Modini et al., 2015; Dedrick et al., 2025) or airborne in situ observations (e.g., Twohy et al., 2005; Modini et al., 2015; Diamond et al., 2018; Kacarab et al., 2020; Gupta et al., 2021; D'Alessandro et al., 2023; Zheng et al., 2024). Airborne platforms allow for higher spatial resolution than satellite 75 observations and greater spatial coverage than ground-based in situ observations.

Marine stratocumulus clouds cover approximately one-third of global oceans (Warren et al., 1988) and have a strong impact on the shortwave radiation budget. ACI and the radiative properties of stratocumulus clouds are regulated in part by cloud top entrainment, which can cause droplet evaporation and thinning of clouds depending on the moisture content of free tropospheric air (Wood, 2012; Mellado, 2017). One region of particular interest for studying these clouds is the Southeast 80 Atlantic Ocean (SEA), where seasonal biomass burning aerosols (BBA) are emitted from Southern Africa and lofted atop a semi-permanent deck of marine stratocumulus clouds (Redemann et al., 2021). The absorbing nature of these aerosols has implications for the direct aerosol radiative effect (DARE; Doherty et al., 2022; Chang et al., 2025), and the entrainment of BBA into both the cloud layer and the underlying marine boundary layer (BL) has implications for cloud microphysical properties (Kaufman et al., 2003; Ross et al., 2003; Adebisi et al., 2015; Zuidema et al., 2016). Diamond et al. (2018) found a 85 strong relationship between in situ N_d and below-cloud BBA in the SEA region. Subsequently, Gupta et al. (2021) found in situ-based evidence of ACI that were dependent on not just below-cloud aerosols, but also the vertical separation between cloud tops and the above-cloud BBA plume. While considerable focus is placed on interactions between below-cloud N_{CCN} and cloud microphysics, recent observational and modelling studies address the possibility of cloud droplet nucleation at cloud-environment interfaces above cloud base (Sun et al., 2012; Hernández Pardo et al., 2019; Oh et al., 2023; Sterzinger and Igel, 90 2024).

The overarching objective of this study is to investigate relationships between stratocumulus cloud properties and N_{CCN} using a remote sensing-based approach. Motivated by the results of Gupta et al. (2021) for the NASA ObseRvations of Aerosols above CLouds and their intEractionS (ORACLES) campaign (Redemann et al., 2021), we expand on this study using remotely-sensed cloud microphysical properties and a new method for retrieving above- and below-cloud N_{CCN} from High 95 Spectral Resolution Lidar 2 (HSRL-2) observables (Redemann and Gao, 2024; Sect. 2.1.1). The use of vertically resolved N_{CCN} from this method allows us to look at ACI as a function of N_{CCN} within 100 m above cloud top and to investigate the



simultaneous impact of above- and below-cloud N_{CCN} on cloud top microphysical properties using lidar profiles adjacent to the cloud edge. Specifically, the research discussed here addresses the following questions:

1. Can remote sensing retrievals replicate the relationships between above-cloud N_{CCN} and cloud top microphysical properties identified from in situ measurements?
2. How do above-cloud ACI vary based on meteorological conditions?
3. Can the impacts of below-cloud N_{CCN} concentration be constrained using retrievals from cloud edge lidar profiles? If so, are above- or below-cloud N_{CCN} more strongly related to cloud top microphysical properties?

2 Data & Methods

The NASA ORACLES campaign was comprised of three deployments in September 2016, August 2017, and October 2018. Deployments were based out of Walvis Bay, Namibia, in September 2016 and São Tomé and Príncipe in August 2017 and October 2018, and observations were made using a combination of remote sensing and in situ instruments located on the NASA P-3 (2016-2018) and the ER-2 (2016 only) aircraft. In this study, results are based on N_{CCN} and cloud microphysical properties retrieved by remote sensing instrumentation. However, we also use two in situ data sets to provide context and prerequisite information for the analysis. Therefore, the remainder of this section is organized as follows. The primary remote sensing-based data sets used in this study are described in Sect. 2.1, in situ data sets are described in Sect. 2.2, and all data sets are summarized in Table 1. Our method for calculating N_{CCN} autocorrelation and using the results to inform data collocation, in addition to the calculation of LTS, are given in Sect. 2.3.

Table 1: List of instruments and data sets used in this study, including their respective resolution, measurement type, and aircraft location.

Instrument	Variables	Resolution (temporal/vertical)	Uncertainty	Measurement Type	Aircraft
High Spectral Resolution Lidar 2 (HSRL-2)	ML-retrieved CCN concentration at supersaturation (S) = 0.4% (cm^{-3}) Cloud top height (CTH; m)	10 s / 15 m	ML-CCN: Within 15 %	Remote Sensing	ER-2 (2016) P-3 (2017-2018)
Research Scanning Polarimeter (RSP)	Cloud droplet effective radius (R_{eff} ; μm)	10 s / 200 m	10 % for both	Remote Sensing	ER-2 (2016) P-3 (2017-2018)



	Cloud optical thickness (COT)				
Cloud condensation nuclei (CCN) counter (DMT CCN-100)	CCN number concentration at different supersaturations (cm^{-3})	1 s	10 %	In Situ	P-3
CAS/CDP	Cloud droplet number concentration (cm^{-3})	1 s	20 %	In Situ	P-3
King hot wire	Bulk liquid water content (g/m^3)	1 s	5 %	In Situ	P-3

2.1 Remote Sensing-Based Data Sets

2.1.1 ML-CCN retrievals from HSRL-2

120 Redemann and Gao (2024) recently developed a machine learning (ML) methodology for retrieving N_{CCN} (ML-CCN) from
 lidar observables, a method which has significant implications for future spaceborne retrievals of N_{CCN} from systems such as
 the Atmospheric LIDar (ATLID) on the EarthCARE satellite (Wehr et al., 2023). The ML algorithm was trained using HSRL-
 2 observables, reanalysis data (temperature and relative humidity), and in situ N_{CCN} from several recent suborbital field
 campaigns and can predict N_{CCN} with mean relative errors of about 15 %. For the ORACLES campaign specifically, the relative
 125 uncertainty of N_{CCN} is evaluated to be approximately 14 % when compared with in situ measurements. In addition to creating
 a larger spatial coverage of N_{CCN} data than is available from the in situ measurements, another benefit is the retrieval of the
 vertical distribution of N_{CCN} possible with this method. This allows us to assess the impact of above- and below-cloud N_{CCN}
 simultaneously from lidar profiles adjacent to cloud edges (Sect. 2.3). Additionally, since relative humidity is one of the
 reanalysis variables used to train the model, cloud edge humidification effects are considered in the prediction of N_{CCN} under
 130 dry conditions (Redemann and Gao, 2024). While Redemann and Gao (2024) use the full suite of HSRL-2 measured
 parameters to predict N_{CCN} , this study uses the same methodology to predict N_{CCN} at a supersaturation of 0.4 % with a model
 that uses backscatter coefficients at 532 and 1064 nm and depolarization ratio at 532 and 1064 nm as input. This combination
 of observables was chosen to maximize the number of available retrievals, as extinction coefficients and all observables at 355
 nm are less frequently available at below-cloud altitudes in the ORACLES observations.



135 2.1.2 Research Scanning Polarimeter

Retrievals of cloud top microphysical properties in this study come from the Research Scanning Polarimeter (RSP), which measures total and polarized reflectance at nine spectral channels (Cairns et al., 1999; Alexandrov et al., 2012a). The RSP is generally oriented to scan along the aircraft track at 0.8° intervals, such that observational data from each scan contains about 150 instantaneous Earth viewing measurements (Alexandrov et al., 2012a). R_{eff} retrievals use polarized reflectance in the scattering angle range between 135° and 165°, where the rain- or cloud-bow structure is observed. Since the rainbow is created by single scattering of light by cloud droplets, the structure is characteristic of droplet sizes at cloud top and within a unit optical depth into the cloud layer, or approximately 50 m (Alexandrov et al., 2018). The RSP R_{eff} retrieval is insensitive to spatial inhomogeneities and three-dimensional radiative transfer effects (Alexandrov et al., 2012b), a significant advantage over satellite retrievals, such as those from MODIS, which tend to overestimate R_{eff} in cases with above-cloud absorbing aerosols (Meyer et al., 2025). The RSP also retrieves cloud optical thickness (COT) using 865 nm unpolarized observations with a 1D radiative transfer model and constraining results using the polarimetric R_{eff} (Alexandrov et al., 2012a; Painemal et al., 2025). While R_{eff} and COT are retrieved quantities and subject to retrieval assumptions and radiative sensitivities, RSP retrievals have been compared and evaluated against in situ observations, demonstrating their accuracy and potential for satellite-based retrievals of this kind, with R_{eff} agreements generally better than 1 μm and effective variance (V_{eff}) agreements better than 0.02 (Alexandrov et al., 2018; Painemal et al., 2021; Fu et al., 2022; Painemal et al., 2025).

From RSP retrievals of R_{eff} and cloud COT, we also calculate N_d and LWP. N_d is calculated using the method from Painemal and Zuidema (2011) given in Eq. (1):

$$N_d = 1.4067e^{-06} \frac{COT^{1/2}}{R_{\text{eff}}^{5/2}}, \quad (1)$$

and LWP is calculated using the method from Wood (2006), as given in Eq. (2):

$$LWP = \frac{5}{9} \rho_w COT R_{\text{eff}}, \quad (2)$$

where ρ_w is the density of water. The calculation of N_d assumes a value of 2.0 g/m³/km for the condensation rate of water vapor with height, which is an average based on observations from the Southeast Pacific of offshore clouds with nearly adiabatic LWC profiles and coastal clouds with decreased LWC at cloud top due to increased entrainment, and thus less adiabatic observed profiles (Painemal and Zuidema, 2010). The relative uncertainties for R_{eff} (Alexandrov et al., 2012a,b) and COT (Nakajima and King, 1990) are both assumed to be 10%, and these values are used in Gaussian error propagation calculations to calculate uncertainties for N_d and LWP, as given in Eqs. (3) and (4), respectively:

$$\delta(N_d) = N_d \left[\frac{1}{4} \left(\frac{\delta(COT)}{COT} \right)^2 + \frac{25}{4} \left(\frac{\delta(R_{\text{eff}})}{R_{\text{eff}}} \right)^2 \right]^{1/2}, \quad (3)$$

$$\delta(LWP) = LWP \left[\left(\frac{\delta(COT)}{COT} \right)^2 + \left(\frac{\delta(R_{\text{eff}})}{R_{\text{eff}}} \right)^2 \right]^{1/2}, \quad (4)$$

where δ represents the error of each variable.



165 2.2 In Situ Data Sets

2.2.1 CCN counter

The Georgia Institute of Technology (GIT) Droplet Measurement Technologies (DMT) CCN counter (CCN-100) measures in situ N_{CCN} at various water vapor supersaturation (Kacarab et al., 2020), which for ORACLES ranged between 0.1 % and 0.4 % (Redemann et al., 2021). The instrument is designed as a continuous-flow streamwise thermal-gradient chamber, where the continuous transport of heat and water vapor from wetted walls is subject to a temperature gradient, which generates quasi-uniform supersaturation in the center of a cylindrical flow chamber (Roberts and Nenes, 2005). Aerosols that activate into droplets with a radius greater than 0.5 μm at the end of the chamber are counted as CCN. The continuous-flow feature allows for quick (1 Hz) sampling, which is important for airborne sampling that often encounters rapidly changing environments (Roberts and Nenes, 2005). N_{CCN} uncertainty is reported as $\pm 10\%$ at high signal-to-noise ratios, while supersaturation uncertainty is given as $\pm 0.04\%$ (Rose et al., 2008). In this study, we use in situ-measured CCN for an autocorrelation analysis to assess over what distances we may reasonably extrapolate cloud edge N_{CCN} values further towards cloud center from the edge (Sect. 2.3-2.4).

2.2.2 In situ cloud probes and cloud base height estimates

To estimate cloud base height, we follow the methodology of Gupta et al. (2021) who derived a relationship between in situ measured cloud top height (Z_T) and cloud base height (Z_B) for six research flights in the 2016 deployment based on the highest and lowest altitudes at which in situ N_d is greater than 10 cm^{-3} and bulk liquid water content (LWC) is greater than 0.05 g/m^3 within sawtooth profiles. We follow their methodology using observations from cloud probes located on the P-3 aircraft during all three ORACLES deployments. Using the resultant statistical relationships between Z_B and Z_T , we estimate cloud base from HSRL-2 cloud top heights (CTH). This method and the resulting cloud base height distribution are described in Appendix A.

185 2.3 Collocation methodology and calculations

2.3.1 Horizontal N_{CCN} autocorrelation

As will be described in more detail in Sect. 3.2, we leverage the vertical resolution of the ML-CCN retrievals to assess the simultaneous impact of both above- and below-cloud N_{CCN} on cloud top microphysical properties by sub-selecting clear-sky profiles that are directly adjacent to profiles that detect a cloud. We assume that N_{CCN} retrieved from the clear profile is approximately equal to N_{CCN} observed below the adjacent cloud. To test the validity of this assumption, we perform an in situ-based autocorrelation analysis to assess the self-consistency of N_{CCN} observed below cloud base heights.

Use of the autocorrelation metric for assessing variability of aerosol properties across various spatial scales has been documented by studies such as Anderson et al. (2003), Heintzenberg et al. (2004), Redemann et al. (2006), Shinozuka and Redemann (2011), Chau et al. (2021), LeBlanc et al. (2022), Perkins et al. (2022), and Franco et al. (2024). Here, we focus on the horizontal variability of N_{CCN} isolated from any effects of vertical variability since we are interested in extrapolating below-

cloud N_{CCN} at a constant altitude from the nearest clear-sky profile. Therefore, the in situ data used to calculate autocorrelation come from constant altitude flight paths where observations do not vary more than ± 25 m in altitude from the first measurement and where data are collected for at least 30 seconds. This minimum time criterion is required to eliminate flight segments where the aircraft may have been slowly ascending or descending through an aerosol layer. Constant altitude flights where the aircraft turns and re-samples an area are split into separate segments. To display autocorrelation as a function of horizontal distance, we convert the original temporal increments to distance using an estimated P-3 aircraft speed of 150 m/s.

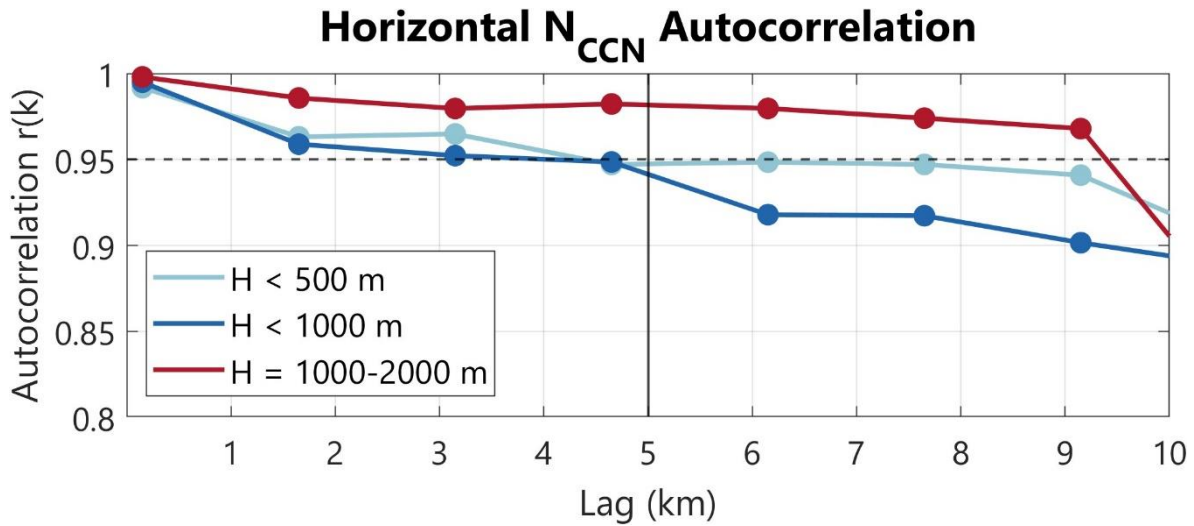


Figure 1: The autocorrelation coefficient of in situ N_{CCN} observed in horizontal flight legs is given as a function of lag distance. The light blue line represents observations from flight legs at altitudes (H) below 500 m, the dark blue line represents observations from flight legs at $H < 1000$ m, and the red line represents observations from flight legs between $H = 1000-2000$ m. The black dashed line depicts an autocorrelation coefficient of 0.95, and the solid vertical line depicts the 5 km over which we assume that below-cloud N_{CCN} is approximately constant.

Data from all constant altitude flight legs are combined and autocorrelation coefficients are calculated at 10 second lag increments (k) between all data pairs y_j and y_{j+k} using Eq. (5):

$$r(k) = \frac{\sum_j^N (y_j - \bar{y}_{+k})(y_{j+k} - \bar{y}_{-k})}{(N-1)\sigma_{+k}\sigma_{-k}}, \quad (5)$$

where $r(k)$ is the autocorrelation coefficient at a given lag, N indicates the number of lagged pairs, y is N_{CCN} , \bar{y}_{+k} and σ_{+k} represent the mean and standard deviation, respectively, of data points located $+k$ away from another data point, and \bar{y}_{-k} and σ_{-k} are the corresponding quantities for data points located $-k$ away from another data point (Anderson et al., 2003).

Since we are interested in the self-consistency of N_{CCN} below cloud base, we calculate autocorrelation for constant altitude flight legs flown at altitudes below 1000 m and at altitudes below 500 m to capture the range of most cloud base heights observed in this analysis (Fig. A1b). We limit in situ N_{CCN} to those with a supersaturation between 0.2-0.4%. This



range captures the supersaturation at which most in situ N_{CCN} observations were made and eliminates significant variation due to changes in supersaturation. Autocorrelation results for all three deployments are given in Fig. 1. We find that assuming that
220 N_{CCN} retrieved from a clear-sky lidar profile is approximately equal to N_{CCN} below cloud base for the adjacent cloudy profile is reasonable, considering the horizontal resolution of these HSRL-2 based profiles is 2 km, at which the autocorrelation coefficient is around 0.96. Additionally, we find that N_{CCN} autocorrelation remains above 0.95, as shown by the dashed line, over a horizontal distance of approximately 5 km.

We also examine N_{CCN} variability above cloud by calculating autocorrelation for constant altitude flight legs flown
225 at altitudes between 1000-2000 m to capture a broad above-cloud range that does not overlap with most cloud base height altitudes (Fig. A1b). We find that over a horizontal range of 5 km the above-cloud autocorrelation coefficient is slightly higher than for below-cloud observations, with it remaining approximately constant around 0.97. Since autocorrelation patterns are similar for above- and below-cloud N_{CCN} , this suggests that across a horizontal range of 5 km, possible impacts of entrainment of BBA into the BL on below-cloud N_{CCN} homogeneity are reflected in the below-cloud N_{CCN} analysis. That is, we do not see
230 rapid decreases in above-cloud N_{CCN} autocorrelation indicative of entrainment mixing that are not reflected in the below-cloud N_{CCN} autocorrelation trends. Therefore, it appears that the BL was often well-mixed and N_{CCN} did not vary significantly across short distances.

This information will be used when collocating both remote sensing-based data sets by assuming that below-cloud
 N_{CCN} is constant over 5 km (Sect. 2.3.2) to increase the number of data points in the analysis. However, this assumption comes
235 with a few caveats. First, the constant altitude flight legs below 500 m and 1000 m likely include both clear-sky and below-cloud observations, and such cases are not differentiated before being included in this analysis. Additionally, those that were observed below-cloud assume that the cloud was non-precipitating. Therefore, the precipitation sink of N_{CCN} below-cloud is not accounted for here and we would expect below-cloud N_{CCN} autocorrelation to be lower if it were included. However, LWP in the following analyses is limited to 80 g/m^2 , and for analyses where we consider below-cloud N_{CCN} it generally falls below
240 40 g/m^2 . Therefore, it is unlikely that precipitation is a major below-cloud N_{CCN} sink within 5 km of cloud edge in these cases. These caveats should be considered when interpreting results involving below-cloud N_{CCN} , but we consider the autocorrelation trends in Fig. 1 to be a general approximation of below-cloud N_{CCN} homogeneity across all ORACLES observations and contend that limiting the constant N_{CCN} assumption to 5 km is reasonable and unlikely to introduce significant errors.

2.3.2 Data collocation and case classifications

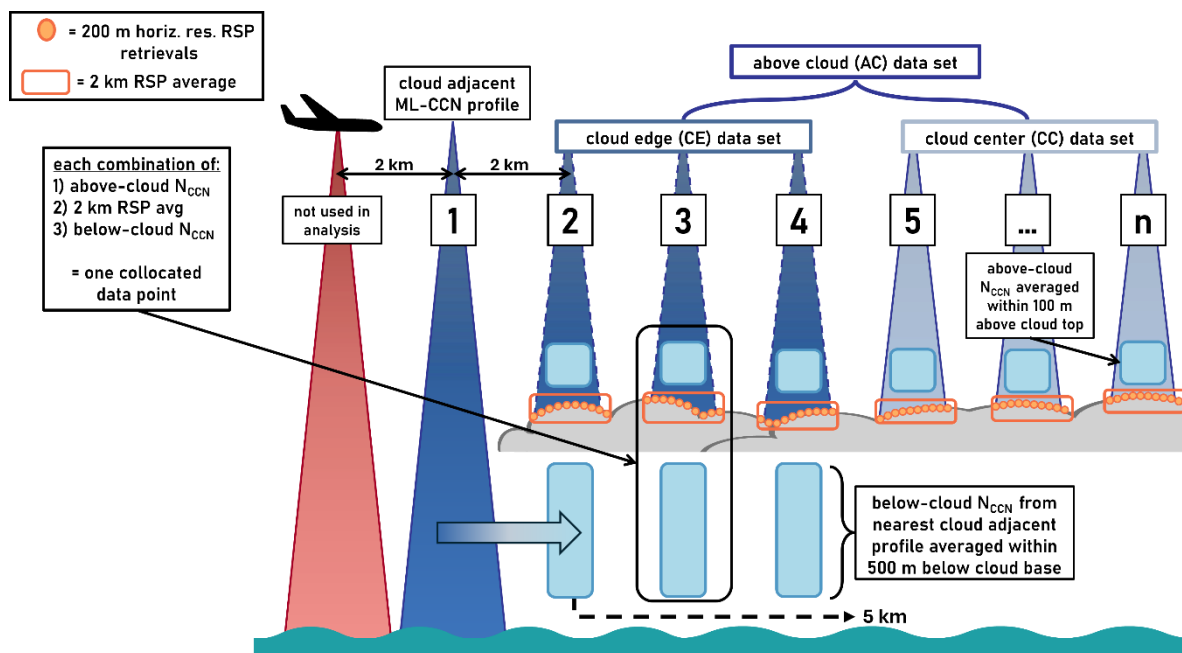
In this study, we define three main subsets of data, all requiring that the aircraft was flying above 2500m and that
245 cloud top heights fall below 2000 m to exclude potential mid- or high-level clouds. The collocation process for these subsets is shown in Fig. 2. To assess the simultaneous impact of above- and below-cloud N_{CCN} on cloud top microphysical properties, we define a subset of the data as cloud edge (CE) cases. These cases are found by first identifying clear-sky, cloud-adjacent ML-CCN profiles. That is, we find clear-sky profiles such as profile 1 in Fig. 2 that are adjacent (2 km) to a profile where the
250 HSRL-2 detects a cloud. We average the N_{CCN} retrieved from profile 1 within a 500 m layer below the cloud base height



determined by profile 2 and thereby determine below-cloud N_{CCN} . We use a 500 m layer to represent overall BL conditions in the below-cloud region. We find coincident RSP retrievals within 10 seconds of the profile 2 measurement, and these are also averaged, resulting in a 2 km RSP average corresponding to the 2 km horizontal resolution of the ML-CCN profile. Additionally, we define above-cloud N_{CCN} as an average of the ML-CCN in profile 2 within 100 m of the cloud top, following the vertical spacing criteria used by Gupta et al. (2021). Therefore, the below-cloud N_{CCN} retrieved from profile 1 is then paired with the cloud top RSP average and above-cloud N_{CCN} associated with profile 2. Additionally, since the in situ autocorrelation analysis indicates that within the BL N_{CCN} maintains an autocorrelation coefficient greater than 0.95 over a horizontal range of 5 km, and thus should remain approximately constant, we extend the same below-cloud N_{CCN} value from profile 1 to additional profiles within 5 km. That is, the below-cloud N_{CCN} value from profile 1 is applied to profiles 2-4, and this approach allows us to approximately triple the number of CE cases in the remainder of the analysis. While profiles 2-4 have the same below-cloud N_{CCN} , the above-cloud N_{CCN} is determined independently for each profile using observations made within 100 m of cloud top height.

For ML-CCN profiles further than 5 km from cloud edge that are associated with an HSRL-2 detected cloud top and have coincident RSP retrievals within 10 seconds, we pair 2 km RSP averages with above-cloud N_{CCN} and call these cloud center (CC) cases, which are represented by profiles 5 through n in Fig. 2, representing the variable nature of the number of cases that may fall in this data set depending on the extent of any given cloud transect. Such cases are only used to assess impacts of above-cloud N_{CCN} , as we do not pair any below-cloud N_{CCN} value with profiles further than 5 km from cloud edge. For analyses in Sect. 3.1 where we focus on relationships between cloud top microphysical properties and above-cloud N_{CCN} , the CE and CC cases are combined into a subset called the above cloud (AC) data set. In Sect. 3.2 we compare the impact of above- and below-cloud N_{CCN} , meaning that only data from the CE data set is considered. And in Sect. 3.3 we investigate the dependence of ACI on proximity to cloud edge by comparing above-cloud observations from CE and CC data sets separately.

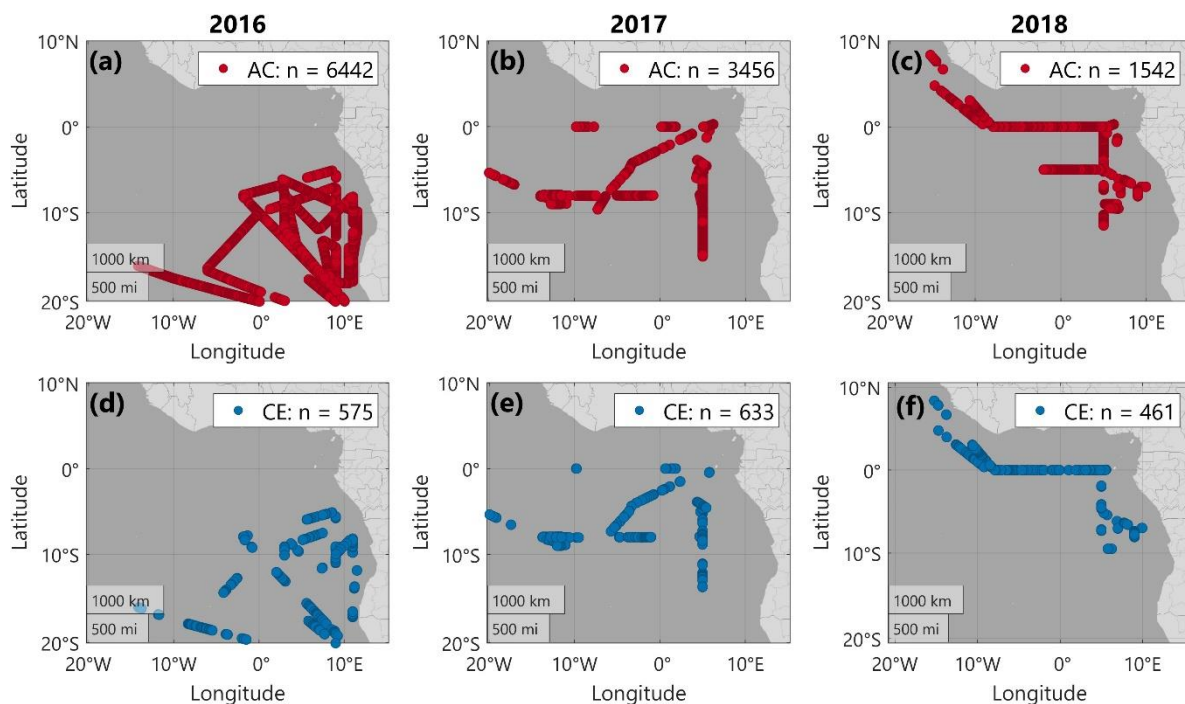
In summary, for the example given in Fig. 2, the paired above-cloud N_{CCN} and RSP measurements from profiles 2 through n would all be included in the AC data set. The above-cloud N_{CCN} , RSP measurements, and below-cloud N_{CCN} in profiles 2-4 are included in the CE data set. Profiles 5 through n do not fall within 5 km of a cloud edge and therefore are included in the CC data set but not the CE data set. Note that these subsets represent a combination of observations from all cloud transects across all three ORACLES deployments and are not in any way grouped by individual cloud profiles. After applying this collocation methodology to observations from all three ORACLES deployments, the location of all cases is given in Fig. 3. Here we find that CE cases are spatially as well-distributed as AC cases. That is, the locations of both cases are very similar, and while the number of CE cases is smaller, they are not limited to any certain geographic area that is not also represented in the AC data set.



285 Figure 2: Collocation schematic depicting above cloud (AC), cloud edge (CE), and cloud center (CC) cases and the collocation of
 ML-CCN profiles with RSP retrievals. Profiles 2 through n are included in the AC dataset (Sect. 3 and 3.1). Profile 1 is the clear-
 sky, cloud-adjacent ML-CCN profile used to determine below-cloud N_{CCN} for adjacent cloudy profiles. Profiles 2-4 are cloudy ML-
 CCN profiles within 5 km of a cloud edge for which above-cloud N_{CCN} is determined from the layer 100 m above cloud top and
 below-cloud N_{CCN} is extrapolated from profile 1, making up the CE cases (Sect. 3.2). Profiles 5 through n are not within 5 km of a
 290 cloud edge and thus are designated as CC cases (Sect 3.3). Profile n represents the variable nature of this collocation process, that is
 that individual cloud transects have differing numbers of observations that fall within the AC and CC cases. The orange outlined
 circles represent each 200 m horizontal resolution RSP retrieval, and the orange boxes around them represent 2 km averages to
 correspond to the 2 km horizontal resolution of the ML-CCN profiles. The red profile represents a ML-CCN profile not adjacent (2
 km) to a cloud.



Above Cloud (AC) and Cloud Edge (CE) Observation Locations



295 **Figure 3: Map depicting the location of (a-c) AC and (d-f) CE cases for 2016 (a, d), 2017 (b, e), and 2018 (c-f) deployments. The number of cases is given in the legend.**

2.3.3 Lower tropospheric stability calculations

To constrain and assess the impact of meteorology and environmental stability on ACI, we calculate lower tropospheric stability (LTS) using temperature profiles from Modern-Era Retrospective analysis for Research and Applications, Version 2 (MERRA-2) data that have been interpolated to HSRL-2 spatiotemporal resolution (Global Modeling And Assimilation Office and Pawson, 2015). LTS is calculated using Eq. (6):

$$LTS = \theta_{800} - \theta_{1000}, \quad (6)$$

where θ is potential temperature at 800 hPa and 1000 hPa. Though LTS is often calculated using potential temperature at 700 hPa, we use 800 hPa to focus on the BL portion relevant for these low clouds and to avoid the aerosol layer around 700 hPa (Adebiyi and Zuidema, 2015; Ryoo et al., 2021). While several approaches have been used to constrain meteorology in previous ACI studies, LTS is a commonly used metric to constrain meteorological effects on clouds (Matsui et al., 2006; Mauger and Norris, 2007; Gryspeerd et al., 2014; Zhang et al., 2016; Jia et al., 2019; Murray-Watson and Gryspeerd, 2022; Zhao et al., 2025).



3 Results

310 We start by investigating the relationships between above-cloud N_{CCN} , R_{eff} , N_d , and LWP for AC cases across all three
ORACLES deployments (Fig. 4). For this analysis we remove data from any cloudy profiles that had a clear-sky profile on
both sides. Such broken cloud regimes are more likely to be impacted by entrainment mixing and evaporation, and here our
focus is on determining aerosol effects on cloud properties. This step reduces the AC data set from 11440 to 11231 profiles.
315 Additionally, we limit observations to those with $LWP \leq 80 \text{ g/m}^2$. This range accounts for most of the ORACLES low cloud
observations, limits scatter from a small number of higher LWP values likely formed under different meteorological conditions,
and reduces the number of precipitating clouds. This step reduces the AC data set from 11231 to 9223 profiles.

For Fig. 4 and those like it in the remainder of Sect. 3, shading on the figures show probability distributions of where
individual data points fall, while the larger scatter points represent an average of each cloud property within N_{CCN} bins of 300
 cm^{-3} . The size of the scatter point is a visual representation of the relative number of data points within each N_{CCN} bin, and the
320 error bars give the average uncertainty of each cloud property within that bin. We calculate ACI metrics to quantify the R_{eff}
(ACI_{REFE}) and N_d (ACI_{CDNC}) response to increasing N_{CCN} following the method described in McComiskey et al. (2009), given
in Eqs. (7) and (8):

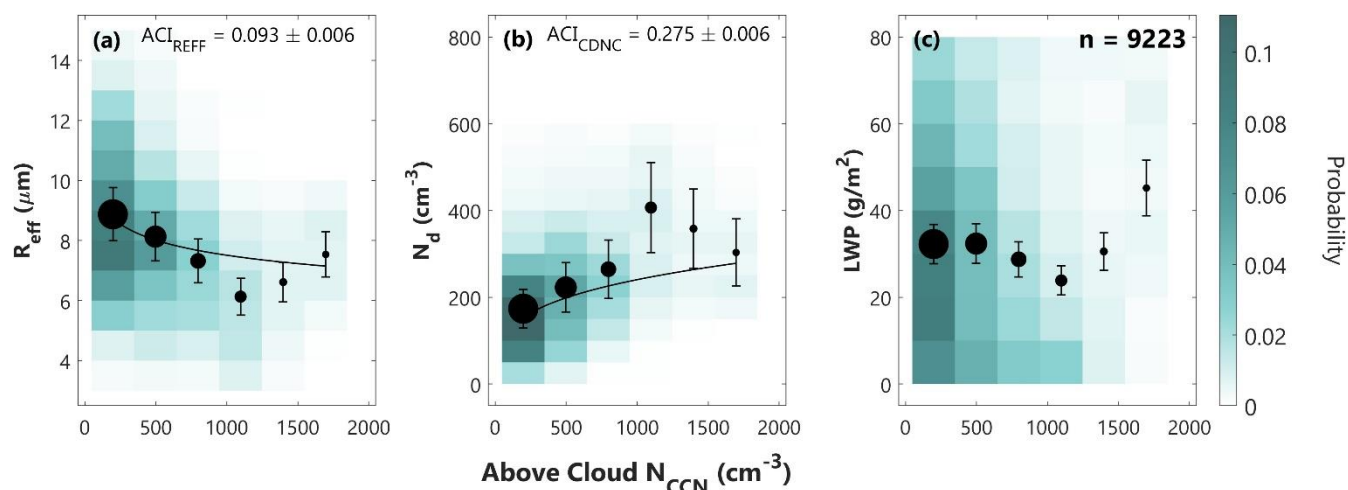
$$ACI_{REFE} = - \left. \frac{\partial \ln(R_{eff})}{\partial \ln(N_{CCN})} \right|_{LWP}, \quad (7)$$

$$ACI_{CDNC} = \frac{d \ln(N_d)}{d \ln(N_{CCN})}. \quad (8)$$

325 These values correspond to the slope of linear regressions calculated for log-transformed R_{eff} , N_d , and N_{CCN} , and these
regressions are calculated for all data points (not the bin averages). The ACI_{REFE} calculation is done within 20 g/m^2 LWP bins,
and the final value is a sample size-weighted average of the individual values calculated for each small LWP range. The error
associated with these metrics are calculated as the standard error (SE) of the slopes via Eq. (9):

$$SE = \sqrt{\frac{\sum_{i=1}^n (y_i - \hat{y}_i)^2 (n-2)}{\sum_{i=1}^n (x_i - \hat{x}_i)^2}}. \quad (9)$$

330 where x represents $\log(N_{CCN})$ and y represents the logarithm of each respective cloud property. These linear regressions
calculated for log-transformed data are also used to plot the corresponding fit lines for R_{eff} and N_d relationships by transforming
the fit equation back into linear space. These fit lines correspond to the full set of data represented by the probability
distributions, not the individual bin averages.



335 **Figure 4: Relationship between above-cloud N_{CCN} and (a) R_{eff} , (b) N_d , and (c) LWP across all three ORACLES deployments. Shading in the background represents the probability of where the 9223 individual data points from this AC data set fall within each panel. Each scatter point is an average within an above-cloud N_{CCN} bin of 300 cm^{-3} . The size of the scatter point represents the number of data points that fall within the bin, and the error bars represent the average uncertainty of the respective cloud property within that bin. ACI metrics and their SE (\pm) are given for R_{eff} and N_d . The fit lines correspond to the slope determined by each ACI metric.**

340 From the combination of data from all three ORACLES deployments, we see clear signals of an above-cloud aerosol influence on the underlying cloud top microphysical properties. As N_{CCN} within the 100 m layer above cloud top increases, there is a decreasing trend in R_{eff} (Fig. 4a) and an increasing trend in N_d (Fig. 4b). ACI_{REFF} is 0.093 and ACI_{CDNC} is 0.275, where the former falls within the 0.04-0.17 range observed for continental stratus clouds by Kim et al. (2008) and the latter falls towards the lower end of the 0.18-0.69 range given for stratocumulus clouds by McComiskey et al. (2009). While LWP is limited to 0-80 g/m^2 , we still see some fluctuations in the LWP as N_{CCN} increases (Fig. 4c), which is an inherent constraint when using observed data. This analysis also allows us to characterize the average properties of low-level stratocumulus clouds in the SEA, as we see that most clouds have R_{eff} values between approximately 7-10 μm , N_d values between 50-250 cm^{-3} , and an LWP between 10-40 g/m^2 . Additionally, in most cases N_{CCN} in the 100 m above cloud top falls below about 750 cm^{-3} . Lastly, for $N_{CCN} > 1000 \text{ cm}^{-3}$ there appears to be a reversal in the cloud property responses, with R_{eff} increasing and N_d decreasing. Nevertheless, the microphysical values in the final bins reflect an overall aerosol influence, with the R_{eff} and N_d for the final bin representing lower and higher values, respectively, when compared to the first bin. These bins appear to have higher average cloud property uncertainties, as is most visible in Fig. 4b, and they represent only a fraction of the data points in lower N_{CCN} bins. This observed pattern reversal and possible physical explanations for it will be discussed further in Sect. 4.

345

350



355 3.1 ACI sensitivity to environmental stability

In this study, we use a k-means clustering approach (Anderberg, 1973) to separate observations of aerosol and cloud properties into different meteorological regimes, as has been done in previous studies (Gryspeerd and Stier, 2012; Gryspeerd et al., 2014; Di Bernadino et al., 2022). This methodology was tested with several combinations of variables including HSRL-2 CTH, RSP-retrieved COT, R_{eff} , N_d , LWP, and MERRA-2 calculated LTS and EIS. All variables were range-standardized before clustering (Milligan and Cooper, 1988), and standard Euclidean distance metrics are used. Various combinations of these variables were compared using Calinski-Harabasz criterion values to determine which combination resulted in the highest between-cluster variance to within-cluster variance ratio (Calinski and Harabasz, 1974). We determined the final number of clusters by maximizing meteorological distinctions among clusters while preserving adequate sample sizes within each to perform statistically meaningful ACI analyses. These testing steps showed that the clusters determined using only LTS had the highest Calinski-Harabasz criterion values, and we determined that using four clusters resulted in adequate sample sizes between clusters for further analysis.

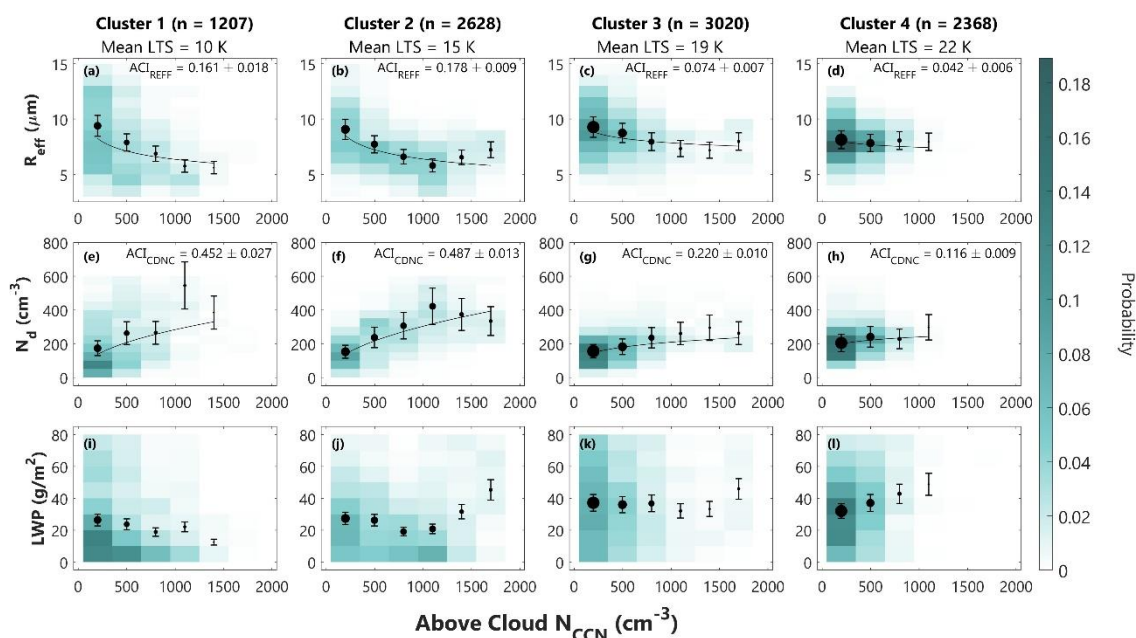


Figure 5: Relationship between above-cloud N_{CCN} and (a-d) R_{eff} , (e-h) N_d , and (i-l) LWP across LTS clusters determined using k-means clustering. The shading, scatter points, ACI metrics, and fit lines are calculated and displayed in the same way as Fig. 4.

370 Previous studies have determined that atmospheric stability is often correlated with stratiform cloud amount (Klein and Hartmann, 1993), and LTS specifically has been used to differentiate between low cloud types in subsidence regimes, such as the SEA (Zhang et al., 2016). Additionally, Zhao et al. (2025) recently found that in high LTS environments, weak entrainment was observed, thus suppressing the negative effects of entrainment observed in environments with low to moderate LTS. While EIS has been suggested to be a better, regime independent predictor of stratus cloud amount than LTS (Wood and



375 Bretherton, 2006), our analysis indicated that using LTS for k-means clustering resulted in higher Calinski-Harabasz criterion values. This could be due to increased uncertainty in the MERRA-2 relative humidity profiles used in the EIS calculation.

This k-means clustering analysis is applied to the same AC dataset as shown in Fig. 4, with results in Fig. 5 given as a function of LTS. Mean LTS ranges from 10 K in cluster 1 to 22 K in cluster 4. As LTS increases, cloud sensitivity to increasing above-cloud N_{CCN} generally decreases, seen as the fit lines become more flat, though ACI metrics increase slightly from cluster 1 to cluster 2 before proceeding to decrease for clusters 3 and 4. This suggests that less stable environments experience increased entrainment mixing, where smoke aerosols located above cloud top are entrained into the cloud and nucleate as cloud droplets. LWP decreases slightly with increasing above-cloud N_{CCN} for lowest LTS (cluster 1) and increases with increasing above-cloud N_{CCN} for highest LTS (cluster 4), while clusters 2 and 3 show mostly constant LWP with an increase for $N_{CCN} > 1000 \text{ cm}^{-3}$. Most observations in cluster 1 are in the northwestern part of the ORACLES region, and observations in cluster 4 are in the southeastern part of the region, closer to the coast (Fig. 6). This corresponds well with average sea surface temperatures (SST) in the SEA, where values generally decrease from northwest to southeast (Ryoo et al., 2021).

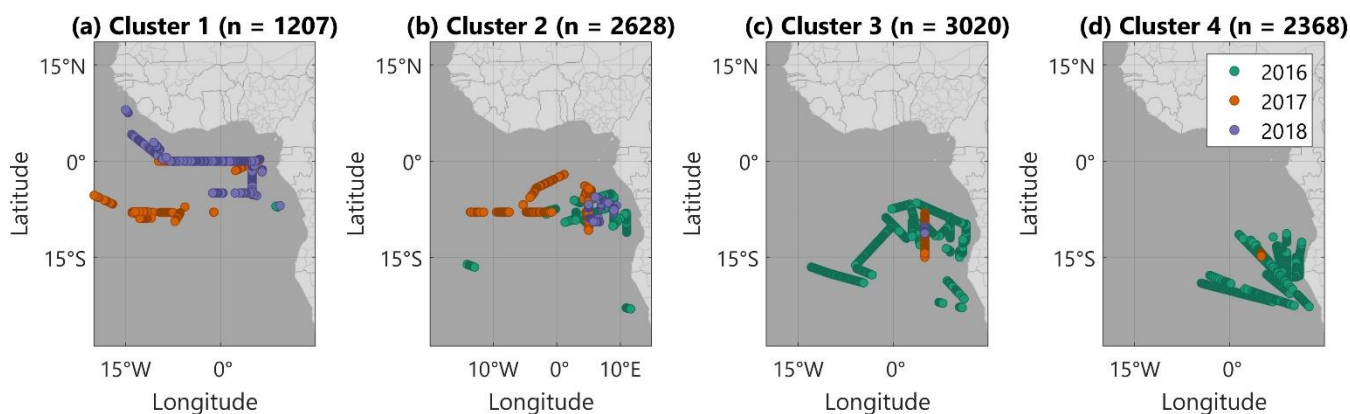


Figure 6: Map showing location of observations in (a) cluster 1, (b) cluster 2, (c) cluster 3, and (d) cluster 4. Average LTS in each cluster increases from left to right. The color of each point corresponds to the deployment year of the observation.

390 Lastly, we show mean values of cloud properties and above-cloud N_{CCN} within each cluster in Table 2. As LTS increases from cluster 1 to 4, average CTH decreases, indicating that a more stable BL is associated with stronger inversions that restrict cloud vertical development (Costantino and Bréon, 2013). Additionally, cluster 2, where the most dense part of the smoke plume was often observed in 2017, has the highest average N_d , smallest average R_{eff} , and highest average above-cloud N_{CCN} , consistent with in situ analyses (Gupta et al., 2022a). Cluster 3 has the lowest average N_d , highest average R_{eff} , and highest average LWP, with values similar to cluster 4. Variability in above-cloud N_{CCN} is high for each cluster, and findings from Lenhardt et al. (2023) suggest that CCN observed across all three campaigns represent a wide range of smoke ages and a small range of aerosol sizes.

Table 2: Mean \pm standard deviation of cloud and aerosol properties within each cluster.



	Cluster 1 (n = 1207)	Cluster 2 (n = 2628)	Cluster 3 (n = 3020)	Cluster 4 (n = 2368)
LTS (K)	10.3 ± 1.3	14.9 ± 1.1	18.5 ± 1.1	22.4 ± 1.3
R _{eff} (μm)	8.3 ± 3.5	7.5 ± 2.4	8.8 ± 2.2	8.0 ± 1.5
N _d (cm ⁻³)	245.4 ± 214.2	273.8 ± 167.4	184.1 ± 91.0	218.2 ± 90.2
LWP (g/m ²)	24.0 ± 21.0	26.2 ± 19.8	36.9 ± 21.4	34.6 ± 19.1
COT	4.8 ± 3.7	5.9 ± 3.9	7.2 ± 3.6	7.4 ± 3.6
CTH (m)	1507.7 ± 387.4	1091.4 ± 249.1	1042.4 ± 171.3	715.0 ± 197.5
Above-Cloud N _{CCN} (cm ⁻³)	454.1 ± 363.3	718.6 ± 465.9	458.8 ± 387.7	315.1 ± 242.0

400

3.2 ACI sensitivity to above- and below-cloud N_{CCN}

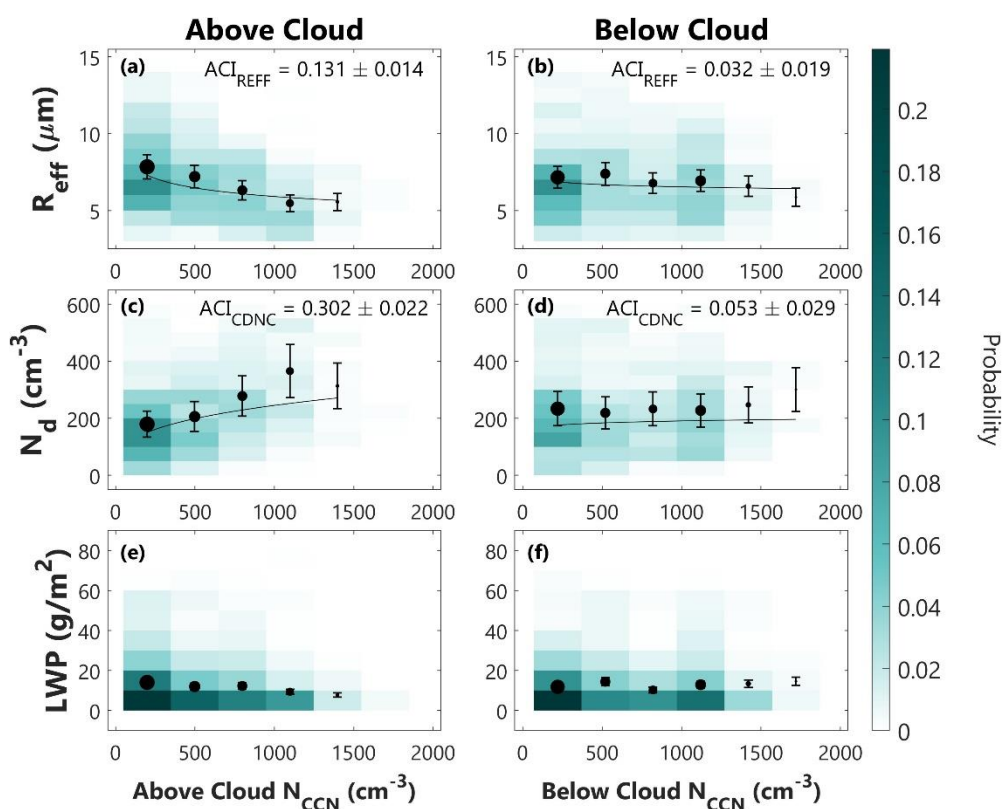


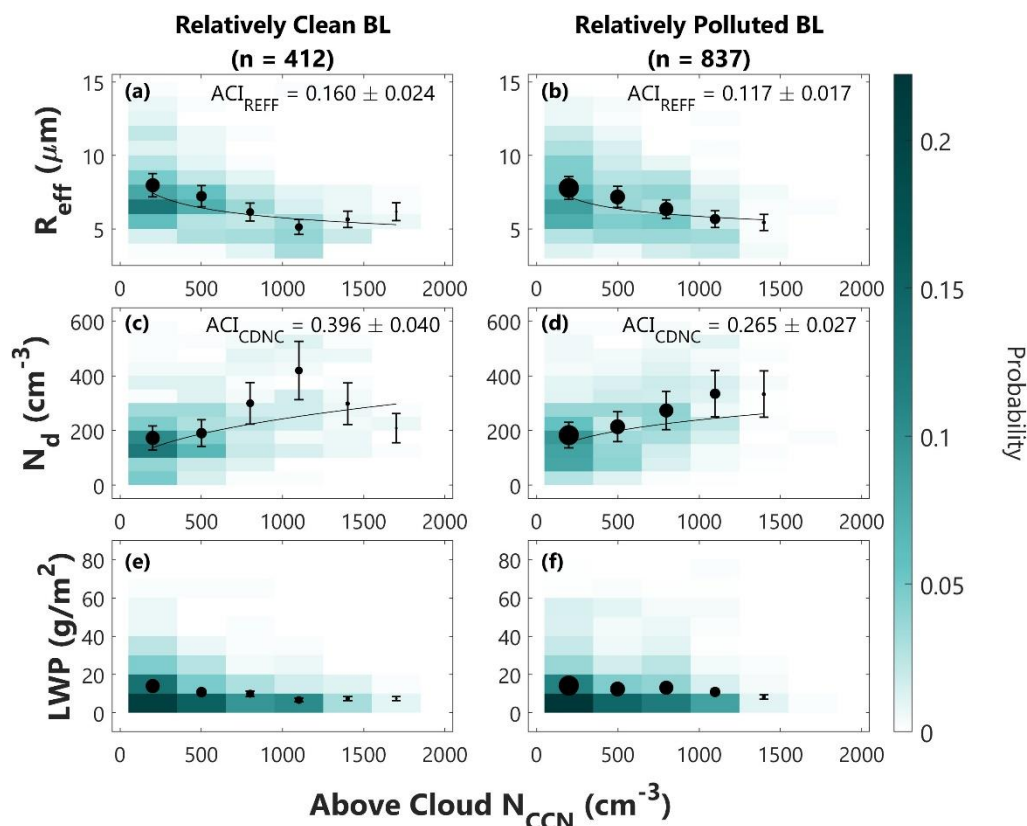
Figure 7: Results of from CE data set (n = 1249) show the relationship between (a, c, e) above- and (b, d, f) below-cloud N_{CCN} and (a-b) R_{eff}, (c-d) N_d, and (e-f) LWP. The shading, scatter points, ACI metrics, and fit lines are calculated and displayed in the same way as Fig. 4.

405 Next, we use the CE data set to investigate the relationships between above- and below-cloud N_{CCN} and R_{eff}, N_d, and LWP.



Here, we again remove cases of cloudy profiles that had a clear profile on both sides to avoid conflating the aerosol effect with effects due to lateral entrainment of ambient air into the cloud layer. This step reduces the CE data set from 1669 to 1269 profiles. Additionally, limiting observations to those with $LWP \leq 80 \text{ g/m}^2$ reduces the CE data set from 1269 to 1249 profiles. Limiting cases to those observed at cloud edge inherently constrains cloud properties, which will be further discussed in Sect. 3.3.

The above-cloud relationships at cloud edge are similar to what was seen from the full AC data set in Fig. 4 and 5. In comparison, the below-cloud N_{CCN} analyses show a weaker relationship to the cloud top microphysical properties, with ACI metrics that are smaller in magnitude compared to the above-cloud metrics. We do not find a strong dependence of the below-cloud N_{CCN} relationships on LTS (Appendix B) as for above-cloud N_{CCN} relationships in the previous section. The range of average N_{CCN} in the 500 m below-cloud is of similar magnitude as N_{CCN} in 100 m above cloud, which is likely evidence of entrainment mixing of BBA from the smoke plume into the BL. Additionally, one major difference from Fig. 4 and 5 is that the range of observed LWP values is much smaller at cloud edge. This will be discussed further in the next section, but a lower LWP does not seem to prohibit observations of above-cloud ACI at cloud edge using this methodology.



420 **Figure 8:** Results of from CE data set ($n = 1174$) show the relationship between above-cloud N_{CCN} and (a-b) R_{eff} , (c-d), N_d , and (e-f) LWP for cases with a relatively clean BL (below-cloud $N_{CCN} \leq 350 \text{ cm}^{-3}$) and a relatively polluted BL (below-cloud $N_{CCN} > 350 \text{ cm}^{-3}$). The shading, scatter points, ACI metrics, and fit lines are calculated and displayed in the same way as Fig. 4.



We also assess the impact of BL aerosol loading on above-cloud ACI relationships by separating the analysis into two cases. Gupta et al. (2021) found that sensitivity to above-cloud aerosol existed regardless of the BL aerosol loading conditions using an aerosol concentration threshold of 350 cm^{-3} . Therefore, in Fig. 8 we show the data from panels a, c, and e of Fig. 7 separated into two cases based on each point's corresponding below-cloud N_{CCN} . Here we are again able to corroborate the results of Gupta et al. (2021). We find that regardless of BL aerosol loading, relationships between above-cloud N_{CCN} and cloud properties are evident. However, we also see that above-cloud ACI_{REF} and ACI_{CDNC} are slightly higher when the below-cloud region is relatively clean. When the below-cloud region is more polluted, above-cloud ACI_{REF} and ACI_{CDNC} are slightly decreased. This dampening of the above-cloud impact for polluted below-cloud regions suggests an impact of below-cloud N_{CCN} on cloud top microphysical properties that is lower in magnitude than the above-cloud N_{CCN} impact but non-zero.

3.3 ACI sensitivity to proximity to cloud edge

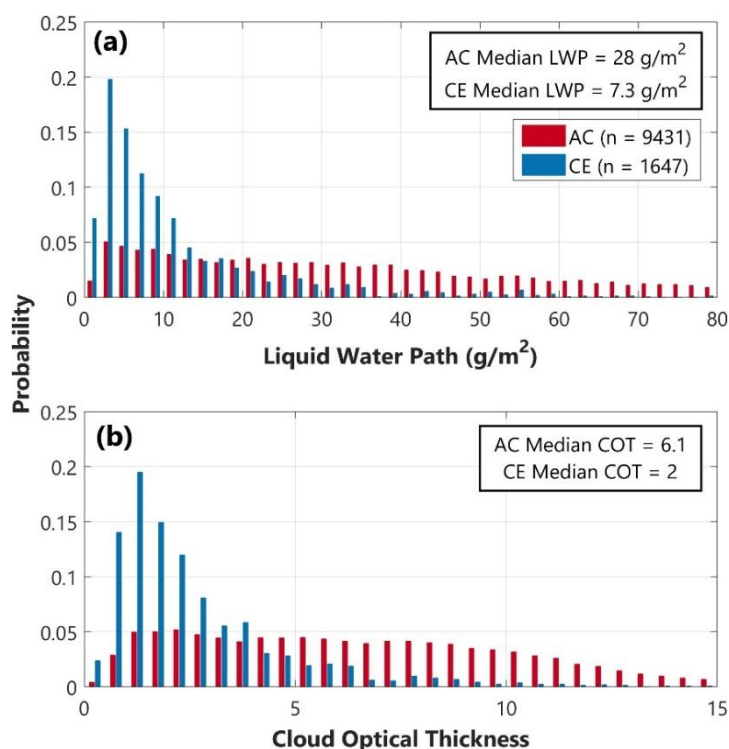


Figure 9: Distributions of (a) LWP and (b) COT for all AC data points (red) and CE data points (blue). Median values for both variables and both subsets of data are also shown

Lastly, we investigate ACI sensitivity to proximity to cloud edge. In the previous two sections we investigated the entire AC data set, which includes observations made anywhere there is a cloud, and the CE data set, which is limited to observations made when a cloudy profile is directly adjacent to a clear profile. Additionally, we have seen that observations in the CE data set are characterized by a lower mean LWP (Fig. 7 and 8) compared to those in the AC data set (Fig. 4 and 5). Here we investigate the differences between cloud edge and cloud center observations, so we no longer exclude cases where a cloudy



440 profile has clear profiles on both sides. Rather, we include them to retain all cloud edge observations in the analysis. The following analyses are still limited to observations made at $LWP \leq 80 \text{ g/m}^2$.

First, we examine differences in LWP and COT between the full AC data set and the CE data set (Fig. 9). This figure reiterates the differences in LWP for observations made at cloud edge, as also seen in Fig. 7 and 8. Cloud edge observations have a median LWP of 7.3 g/m^2 while the entire AC data set has a median LWP of 28 g/m^2 . We see similar differences in
 445 COT, where the median COT at cloud edge is 2.0 compared to a median value of 6.1 for the full AC data set. Observations made for the full AC data set also have a much broader distribution in both LWP and COT than those made at cloud edge.

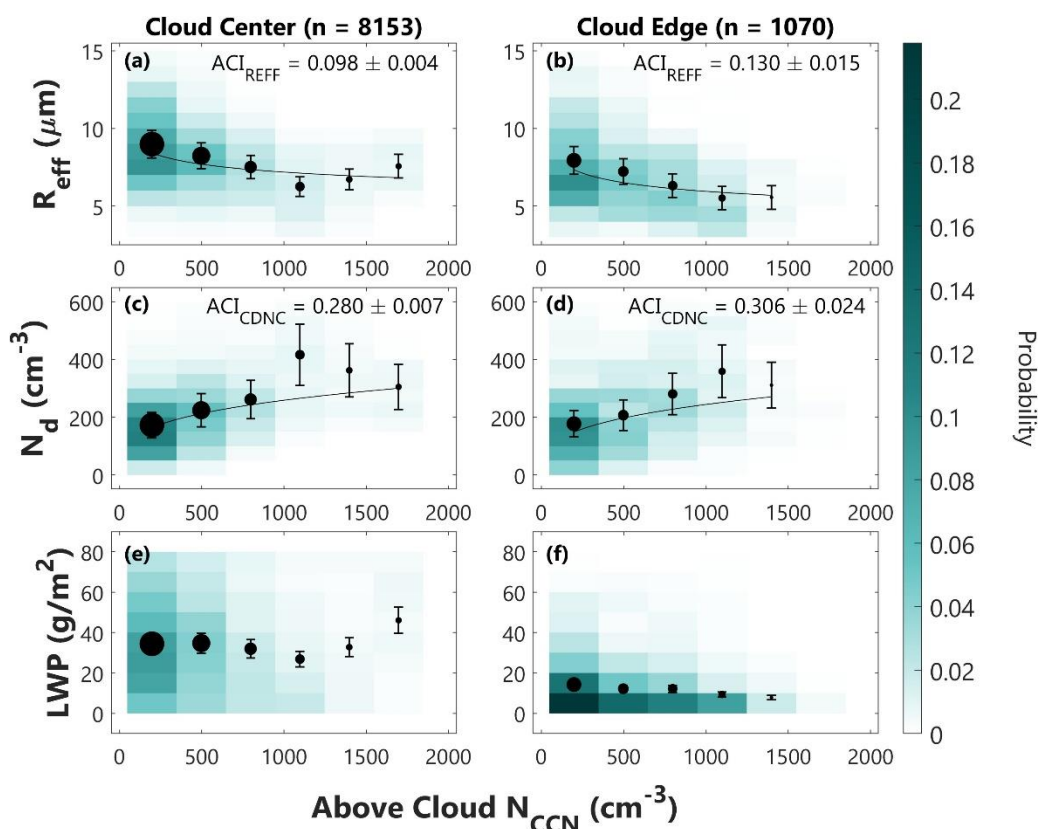


Figure 10: Results from cloud center and CE data sets show the relationship between above-cloud N_{CCN} and (a-b) R_{eff} , (c-d) N_d , and (e-f) LWP. The shading, scatter points, ACI metrics, and fit lines are calculated and displayed in the same way as Fig. 4.

To investigate if lower LWP and COT at cloud edge are associated with any differences in ACI_{REFF} and ACI_{CDNC} , we
 450 compare results between CE and CC cases (Fig. 10). Like the comparison between cases with relatively clean and polluted BL conditions (Fig. 8), we see that regardless of whether observations are made closer to the center of a cloud or at a cloud edge, the relationships between above-cloud N_{CCN} and cloud top R_{eff} and N_d are similar, with ACI metrics being slightly higher for the cloud edge observations than cloud center observations. This suggests that while increased mixing and entrainment of smoke aerosols into the cloud and nucleation of additional cloud droplets is observed for all cases, it may be occurring more
 455 frequently at cloud edges. Furthermore, while we do not have below-cloud N_{CCN} for CC cases using this methodology, the



similarity in above-cloud N_{CCN} relationships at cloud center and cloud edge could imply that below-cloud N_{CCN} relationships may also be similar in these two regimes. However, further investigation of below-cloud N_{CCN} relationships towards cloud center would likely require modelling efforts or dependence on in situ observations and is beyond the scope of this study.

4 Discussion

460 In our remote sensing-based analysis of ACI between BBA and the underlying stratocumulus cloud deck in the SEA, we have investigated the relationships between above- and below-cloud N_{CCN} and cloud top microphysical properties as a function of environmental stability, below-cloud aerosol loading, and proximity of observations to the cloud edge. In this section we will further discuss the physical relationships seen in the observations (Sect. 4.1) and implications for future remote sensing of ACI (Sect. 4.2).

465 4.1 Physical relationships

Overall, the relationships analyzed here follow the major findings of Gupta et al. (2021), around which this study was formulated. That is, for cases where the smoke plume is in contact with the cloud top, there is evidence of these CCN impacting cloud top microphysical properties. For all cases, increases in above-cloud N_{CCN} were associated with increases in N_d and decreases in R_{eff} . Cases of contact between cloud top and the BBA plume are associated with greater entrainment mixing (Diamond et al., 2018; Gupta et al., 2021), and our finding here reiterates those suggesting that entrainment of BBA that serve as CCN can result in nucleation of cloud droplets near the cloud top. Additionally, we found relatively weak relationships between below-cloud N_{CCN} and cloud top microphysical properties, but an indication that polluted BL conditions were associated with a dampened above-cloud N_{CCN} impact. However, it is important to consider that the above- and below-cloud N_{CCN} comparisons in this study were limited to observations within 5 km of cloud edge, and thus they may not be perfectly representative of below-cloud N_{CCN} impacts closer to cloud center. Future work should focus on better elucidating this relatively weak impact of below-cloud N_{CCN} compared to above-cloud N_{CCN} .

One major focus of this study was the dependence of aerosol – cloud relationships on environmental stability. Based on a k-means clustering analysis using LTS as the sole clustering variable, we stratified observations of the cloud deck with collocated above-cloud N_{CCN} retrievals into four clusters which turn out to be geographically distinct, with LTS increasing from the northwestern part of the SEA toward the southeastern part closest to the African coast. This increase in LTS aligns well with observed decreases in SST and CTH. By constraining the meteorology, we find that environmental stability is an important governing factor in determining the sensitivity of cloud properties to increases in above-cloud N_{CCN} . As the atmosphere becomes more stable, cloud sensitivity to increasing above-cloud N_{CCN} decreases until there is almost no response (cluster 4; Fig. 5d, h). This suggests that less stable environments promote greater vertical growth of the cloud layer and mixing led by cloud top entrainment instability (e.g., Mellado, 2017; Gupta et al., 2021). This environment thereby supports the modulation of cloud top properties by aerosols from the overlying smoke plume that are entrained into the cloud layer. The



percent differences in ACI metrics between cluster 4 and cluster 1 are -73.9 % for ACI_{REF} and -74.3 % for ACI_{DNC} , again indicating that ACIs depend strongly on environmental conditions. While we see from Fig. 4 that above-cloud ACIs are evident across the full data set, stratifying the data by LTS demonstrates the significant role that meteorology plays in determining how clouds respond to increases in above-cloud N_{CCN} . For example, comparing the full data set (Fig. 4a,b) to the cluster of data with the lowest mean LTS (Fig. 5a,e) ACI_{REF} increases from 0.093 to 0.161 (73.1 %) and ACI_{DNC} increases from 0.275 to 0.452 (64.4 %). Therefore, stratifying data by environmental stability has a large impact on the magnitude, and arguably the accuracy, of the ACI metrics. These stability-related findings corroborate those from additional ORACLES ACI-focused studies. Using ORACLES 2016 in situ observations, Diamond et al. (2018) found a weaker relationship between cloud properties and above-cloud BBA compared to the below-cloud effect, and similarly a majority of the 2016 observations in this study are categorized by a high average LTS (Fig. 6), where we see above-cloud ACI relationships begin to weaken. Kacarab et al. (2020) discussed sensitivity of ACI to velocity-limited and aerosol-limited regimes in the ORACLES 2017 observations, and this analysis indirectly suggests a dependence on updraft velocity via environmental stability. Future work exploring differences in aerosol properties, cloud properties, and other meteorological variables within each of these clusters could further assess and constrain ACI in this region.

There are small scale variations evident in the bin averages that are not significantly reflected in the fit lines and therefore are not a primary focus of this analysis. However, in Fig. 4a and 4b, as well as Fig. 5b and 5f, we see slight reversals in the expected patterns for R_{eff} and N_d for above-cloud $N_{CCN} > 1000 \text{ cm}^{-3}$. These bin averages have fewer data points and slightly higher mean uncertainty than those at lower N_{CCN} , meaning that this switch to increasing R_{eff} and decreasing N_d for high above-cloud N_{CCN} could be an artifact of uncertainty and limited data. However, here we will discuss a few alternative hypotheses based on previous literature. For example, considering this pattern only occurs at $N_{CCN} > 1000 \text{ cm}^{-3}$, indicating significant contact between cloud top and the smoke plume, one hypothesis for this pattern could be the aerosol semi-direct effect, which describes how absorbing aerosols may act to change cloud properties (Hansen et al., 1997). A study by Koch and Del Genio (2010) that focused on the proximity of absorbing aerosol to different cloud types found that stratocumulus clouds with absorbing aerosol near the cloud top are likely to experience cloud reduction due to the semi-direct effect. Other studies have found a positive correlation between high aerosol loading and cloud droplet size in highly polluted environments without directly characterizing it as the semi-direct effect (Tang et al., 2014; Ma et al., 2018; Jose et al., 2020; Khatri et al., 2022). One commonly proposed pathway is that the aerosol radiative effect reduces moisture content and increases competition for water vapor, causing smaller droplets to evaporate, which could explain the decrease in N_d and increase in R_{eff} . This pattern would also align well with the findings of Kacarab et al. (2020), where ORACLES 2017 in situ observations showed no response in N_d to increasing aerosol concentration $> 800 \text{ cm}^{-3}$ when water vapor was limited.

Alternatively, these patterns could indicate that at $N_{CCN} > 1000 \text{ cm}^{-3}$ the environment is saturated by such a large number of small droplets that they begin to coalesce and form precipitation, thus forming fewer droplets that are larger in size. Such a decrease in precipitation susceptibility has been associated with an increase in LWP (Sorooshian et al., 2009), which is also associated with increasing R_{eff} and decreasing N_d here (Fig. 4c and Fig. 5j). However, untangling the response of LWP to



aerosols compared to meteorology is difficult, with many proposed pathways by which LWP may increase or decrease in response to increased aerosol loading (Gryspeerd et al., 2019). More detailed process modelling would likely be needed to fully understand and untangle the relationships and cause-and-effect pathways between above-cloud N_{CCN} and cloud top R_{eff} , N_d , and LWP for these cases of increased above-cloud aerosol loading, which is outside the scope of this study. Therefore, we
525 hypothesize that the reversal of R_{eff} and N_d trends at high above-cloud N_{CCN} could be indicative of a semi-direct effect due to BBA absorption or the beginning of collision-coalescence due to a highly saturated environment.

4.2 Implications for remote sensing techniques

The major implication of these results confirming those of an in situ-based study (Gupta et al., 2021) is that ACI can reliably be estimated using only these remote sensing-based observations. We make use of well-located HSRL-2 and RSP
530 observations from the ORACLES campaign to investigate relationships between cloud microphysical properties and vertically resolved N_{CCN} both above- and below-cloud. This strategy not only corroborates in situ-based findings using a larger amount of data than is available from in situ observations, but it also demonstrates a methodology that can be used with current and future satellite-based observations.

As previously mentioned, the vertical distribution of N_{CCN} is especially relevant for understanding ACI. For the
535 ORACLES region, where we have the unique scenario of an optically thick and strongly absorbing BBA plume overlying marine stratocumulus clouds, we found that changes in above-cloud N_{CCN} are more strongly related to changes in cloud top microphysical properties than the below-cloud N_{CCN} . However, without vertically resolved N_{CCN} from the ML-CCN method, this distinction would not have been possible. Additionally, the high accuracy of the ML-CCN method has an advantage over other active spaceborne sensors such as CALIOP that have routinely misplaced the vertical extent of aerosol plumes and thus
540 misrepresented ACI (Rajapakshe et al., 2017). Another benefit of the ML-CCN method is that it allows us to use data in close proximity (2 km) to cloud edge without concerns about cloud edge humidification effects since environmental relative humidity is considered in the model training. A similar methodology as that shown here could be done in other regions using Atmospheric LIDar (AtLID) and Multi Spectral Imager (MSI) observations from the recently launched EarthCARE satellite (Wehr et al., 2023) in combination with other satellite-based cloud retrievals. While higher uncertainty and lower signal-to-
545 noise may be associated with AtLID N_{CCN} retrievals, the overall framework presented here remains valid for spaceborne remote sensing of ACI. Lastly, the dependence of cloud sensitivity to increasing above-cloud N_{CCN} on LTS speaks to the need to constrain future satellite observations by a parameter such as LTS to accurately represent meteorological impacts on ACI metrics, which may also impact their parameterization in models.

5 Conclusions

550 One key component missing from several studies of ACI is the vertical distribution of N_{CCN} relative to cloud height, which in regions with significant tropospheric aerosol loading is critical to understanding how and where aerosols are nucleating as



cloud droplets and impacting cloud microphysical properties. Here we use a fully remote sensing-based data set to investigate
ACI over the SEA using HSRL-2-based, ML-predicted N_{CCN} curtains and cloud microphysical properties retrieved from the
RSP. To assess the simultaneous above- and below-cloud impact of N_{CCN} on cloud properties, we infer below-cloud N_{CCN}
555 values from cloud-edge adjacent profiles. Previous in situ-based studies have found evidence of ACI between smoke plume
BBA and the underlying stratocumulus cloud deck. Therefore, the major goals of this study were to investigate these cloud top
ACI in more detail and to determine whether such relationships could be observed using only remote sensing data.

We found that our results align well with those of the in situ-based study (Gupta et al., 2021). That is, we see a
decrease in R_{eff} and increase in N_d when the BBA concentrations are significant within 100 m of the cloud top, and this finding
560 is independent of horizontal proximity to cloud edge. Using clear-sky, cloud-adjacent ML-CCN profiles, we examine the
simultaneous impact of above- and below-cloud N_{CCN} and find that the relationship between cloud top microphysical properties
and above-cloud N_{CCN} is stronger than their relationship with below-cloud N_{CCN} . This finding is independent of the magnitude
of BL aerosol loading. Therefore, it appears that entrainment of BBA at cloud top in the SEA is a major control of cloud top
microphysical properties. However, the dominance of this effect in comparison to that of below-cloud N_{CCN} remains an open
565 question that would likely require modelling studies to further assess. Additionally, to constrain the impact of meteorology we
cluster the above-cloud data set by LTS, finding that cloud sensitivity to increasing above-cloud N_{CCN} decreases as LTS
increases. The strongest $R_{eff} - N_{CCN}$ and $N_d - N_{CCN}$ relationships are found in the northwestern part of the ORACLES region
where average LTS is around 10 K, and the relationships weaken moving southeast towards the African coast. Therefore, while
we do see evidence of an aerosol effect on cloud properties, this effect is highly dependent on environmental stability.

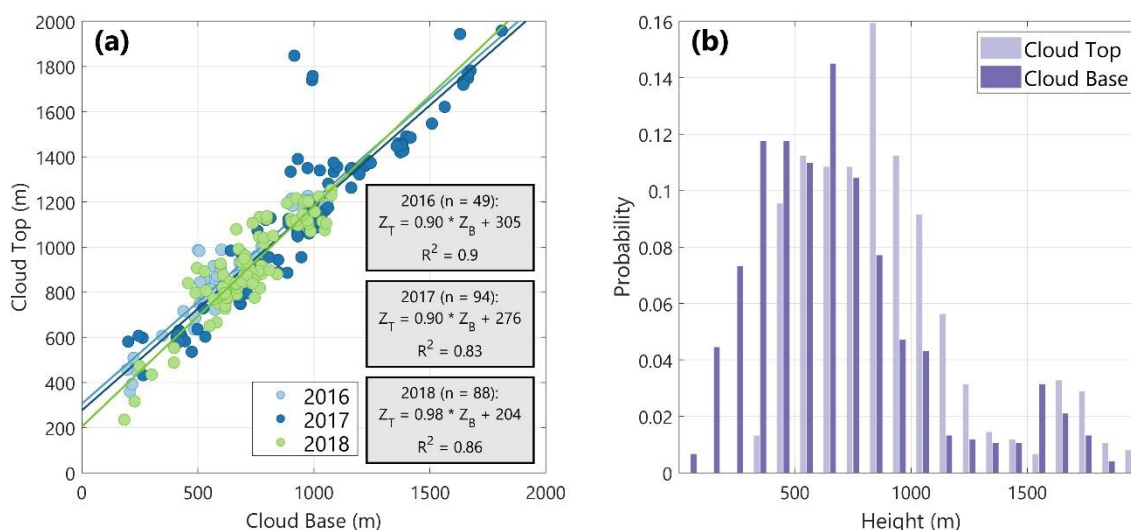
A major implication of this work is the ability to assess ACI using remote sensing-based observations, a method that
can be applied to current and future spaceborne observations. We have demonstrated the benefit of the Redemann and Gao
(2024) ML-CCN product in that it can be used to separate the impact of above- and below-cloud N_{CCN} on cloud properties in
the same column. Additionally, we have used autocorrelation analyses to characterize the variability of N_{CCN} in the SEA BL,
which provides a tool to extrapolate clear-sky N_{CCN} retrievals to nearby clouds. We concede that this extrapolation carries its
575 own uncertainty, but it is superior to the inherent spatial homogeneity assumptions in ACI studies that derive ACI metrics
from large-scale averaged satellite retrievals of aerosol and cloud properties. Each of these methodologies can be applied to
future studies in different regions and cloud types to further work toward reducing uncertainty associated with the radiative
impacts of ACI.

580 Appendix A

As in Gupta et al. (2021), relationships between cloud top height (Z_T) and cloud base height (Z_B) are developed from in situ
data including the Cloud and Aerosol Spectrometer (CAS) on the Cloud, Aerosol and Precipitation Spectrometer (CAPS;
Baumgardner et al., 2001), two Cloud Droplet Probes (CDP; Lance et al., 2010), and a King hot-wire (King et al., 1978). The
King hot-wire was used to determine bulk liquid water content (LWC). CAS and the CDP measured the cloud droplet size
585 distribution, and the full size distribution spectrum covering diameters between 3-50 μm was determined using the probe most



consistent with the King hot-wire LWC (Gupta et al., 2022a). These observations are used to find the highest (cloud top) and lowest (cloud base) altitudes within individual sawtooth profiles at which in situ cloud N_d is greater than 10 cm^{-3} and bulk liquid water content (LWC) is greater than 0.05 g/m^3 . Our resulting linear relationships between in situ Z_T and Z_B are shown in Figure A1a. We then estimate cloud base height from HSRL-2 cloud top heights using these statistical relationships developed from in situ observations. When this method is applied to each lidar profile observed at a cloud edge (Sect. 2.4), we find that most cloud base heights fall between about 400-750 m (Fig. A1b).



595 **Figure A1: (a) In situ derived relationship between cloud top height (Z_T) and cloud base height (Z_B) based on the methodology of Gupta et al. (2021). These relationships are applied to HSRL-2 cloud top heights measured at cloud edge for all three deployment years of ORACLES. The distributions of these HSRL-2 measured cloud top heights and resultant calculated cloud base heights are given in panel (b).**

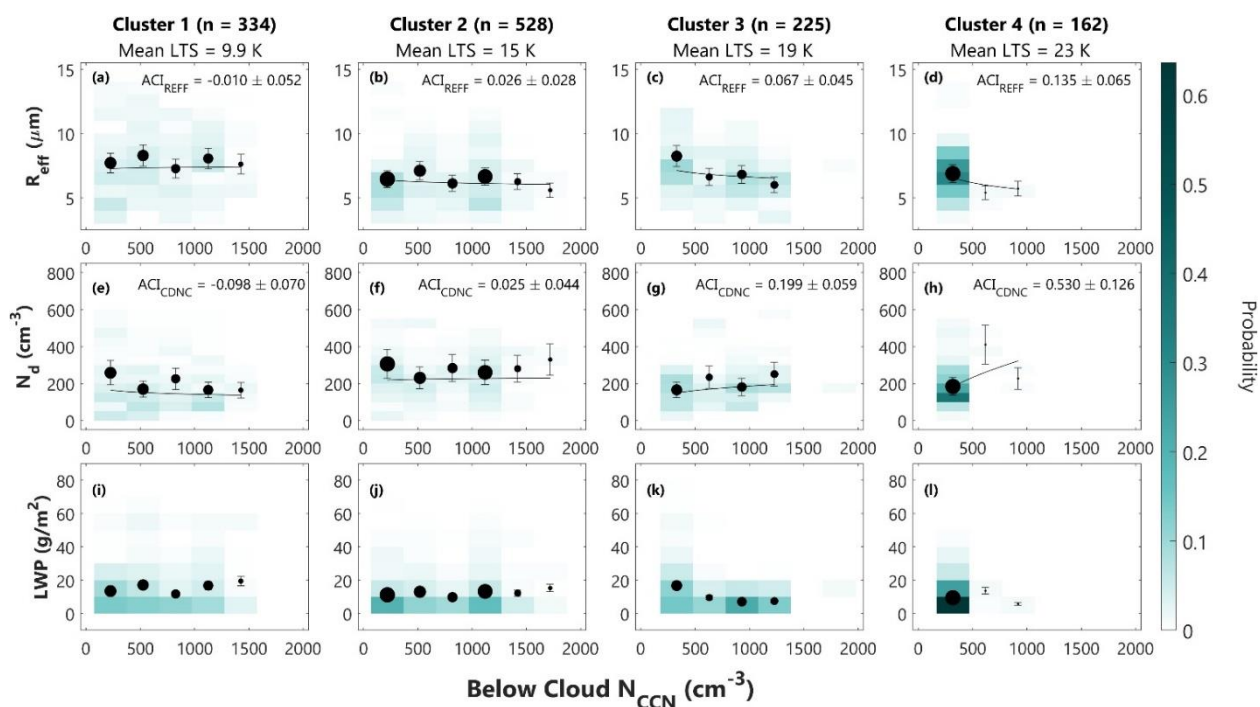
Appendix B

600 To test the dependence of the below-cloud N_{CCN} relationships on LTS, we assign observations from the CE data set to the clusters defined in Fig. 5 and 6 (Fig. B1). Unlike the AC data set, we do not find a strong dependence of the below-cloud N_{CCN} relationships with R_{eff} and N_d on LTS. Though data in cluster 4 appears to have stronger relationships than those in the first three clusters, this cluster is limited to a very small number of data points, where most fall in a single CCN bin. Therefore, we conclude that the patterns seen for the full set of below-cloud N_{CCN} in Fig. 7 are representative and do not mask any LTS-related dependencies.

605



610



615 **Figure B1:** Below-cloud observations from Fig. 7 are assigned to clusters determined in Fig. 5. Results of this clustering show the relationship between below-cloud N_{CCN} and (a-d) R_{eff} , (e-h) N_d , and (i-l) LWP. Average LTS in each cluster increases from left to right. The shading, scatter points, ACI metrics, and fit lines are calculated and displayed in the same way as Fig. 5.

Data Availability

620 The ER-2 and P-3 data sets are available at the following links: https://doi.org/10.5067/Suborbital/ORACLES/P3/2016_V3 (ORACLES Science Team, 2021a), https://doi.org/10.5067/Suborbital/ORACLES/ER2/2016_V3 (ORACLES Science Team, 2021b), https://doi.org/10.5067/Suborbital/ORACLES/P3/2017_V3 (ORACLES Science Team, 2021c), and https://doi.org/10.5067/Suborbital/ORACLES/P3/2018_V3 (ORACLES Science Team, 2021d). Machine learning-predicted N_{CCN} data is available at: <https://doi.org/10.5281/zenodo.18626083> (Gao et al., 2026).

625

Author Contributions

EDL, LG, and JR formulated the science questions and corresponding analyses. EDL organized all data products, performed analyses, visualized the results, and wrote the draft. LG, SG, GM, FX, RAF, CAH, and JR edited the manuscript and provided insightful discussion and suggestions.

630

Competing Interests

At least one of the (co-)authors is a member of the editorial board of Atmospheric Chemistry and Physics.

Acknowledgements

635 We would like to thank the entire NASA ORACLES science team in addition to the P-3 and ER-2 pilots and flight crews for a successful deployment. In addition, we acknowledge contributions from the HSRL-2, CCN, and RSP instrument teams. Emily D. Lenhardt acknowledges support from NASA FINESST grant 80NSSC24K0008. Siddhant Gupta is supported by Argonne National Laboratory under U.S. DOE contract DE-AC02-06CH11357 and the ARM User Facility, funded by the Office of Biological and Environmental Research in the U.S DOE Office of Science.

640

Financial Support

This research has been supported by the National Aeronautics and Space Administration (grant no. 80NSSC24K0008).

References

- 645 Adebisi, A. A. and Zuidema, P.: The role of the southern African easterly jet in modifying the southeast Atlantic aerosol and cloud environments, *Q.J.R. Meteorol. Soc.*, 142, 1574–1589, <https://doi.org/10.1002/qj.2765>, 2016.
- Adebisi, A. A., Zuidema, P., and Abel, S. J.: The Convolution of Dynamics and Moisture with the Presence of Shortwave Absorbing Aerosols over the Southeast Atlantic, *Journal of Climate*, 28, 1997–2024, <https://doi.org/10.1175/JCLI-D-14-00352.1>, 2015.
- 650 Alam, K., Iqbal, M. J., Blaschke, T., Qureshi, S., and Khan, G.: Monitoring spatio-temporal variations in aerosols and aerosol–cloud interactions over Pakistan using MODIS data, *Advances in Space Research*, 46, 1162–1176, <https://doi.org/10.1016/j.asr.2010.06.025>, 2010.
- Albrecht, B. A.: Aerosols, Cloud Microphysics, and Fractional Cloudiness, *Science*, 245, 1227–1230, <https://doi.org/10.1126/science.245.4923.1227>, 1989.
- 655 Alexandri, F., Müller, F., Choudhury, G., Achtert, P., Seelig, T., and Tesche, M.: A cloud-by-cloud approach for studying aerosol–cloud interaction in satellite observations, *Atmos. Meas. Tech.*, 17, 1739–1757, <https://doi.org/10.5194/amt-17-1739-2024>, 2024.



- Alexandrov, M. D., Cairns, B., Emde, C., Ackerman, A. S., and Van Diedenhoven, B.: Accuracy assessments of cloud droplet size retrievals from polarized reflectance measurements by the research scanning polarimeter, *Remote Sensing of Environment*, 125, 92–111, <https://doi.org/10.1016/j.rse.2012.07.012>, 2012a.
- 660 Alexandrov, M. D., Cairns, B., and Mishchenko, M. I.: Rainbow Fourier transform, *Journal of Quantitative Spectroscopy and Radiative Transfer*, 113, 2521–2535, <https://doi.org/10.1016/j.jqsrt.2012.03.025>, 2012b.
- Alexandrov, M. D., Cairns, B., Sinclair, K., Wasilewski, A. P., Ziemba, L., Crosbie, E., Moore, R., Hair, J., Scarino, A. J., Hu, Y., Stamnes, S., Shook, M. A., and Chen, G.: Retrievals of cloud droplet size from the research scanning polarimeter data: Validation using in situ measurements, *Remote Sensing of Environment*, 210, 76–95, <https://doi.org/10.1016/j.rse.2018.03.005>, 2018.
- 665 <https://doi.org/10.1016/j.rse.2018.03.005>, 2018.
- Anderberg, M.: *Cluster Analysis for Applications*, Elsevier, <https://doi.org/10.1016/C2013-0-06161-0>, 1973.
- Anderson, T. L., Charlson, R. J., Winker, D. M., Ogren, J. A., and Holmén, K.: Mesoscale Variations of Tropospheric Aerosols*, *J. Atmos. Sci.*, 60, 119–136, [https://doi.org/10.1175/1520-0469\(2003\)060%253C0119:MVOTA%253E2.0.CO;2](https://doi.org/10.1175/1520-0469(2003)060%253C0119:MVOTA%253E2.0.CO;2), 2003.
- 670 Andreae, M. O.: Smoking Rain Clouds over the Amazon, *Science*, 303, 1337–1342, <https://doi.org/10.1126/science.1092779>, 2004.
- Andreae, M. O.: Correlation between cloud condensation nuclei concentration and aerosol optical thickness in remote and polluted regions, *Atmos. Chem. Phys.*, 9, 543–556, <https://doi.org/10.5194/acp-9-543-2009>, 2009.
- Baumgardner, D., Jonsson, H., Dawson, W., O’Connor, D., and Newton, R.: The cloud, aerosol and precipitation spectrometer: a new instrument for cloud investigations, *Atmospheric Research*, 59–60, 251–264, [https://doi.org/10.1016/S0169-8095\(01\)00119-3](https://doi.org/10.1016/S0169-8095(01)00119-3), 2001.
- 675 Cairns, B., Russell, E. E., and Travis, L. D.: Research Scanning Polarimeter: calibration and ground-based measurements, SPIE’s International Symposium on Optical Science, Engineering, and Instrumentation, Denver, CO, 186–196, <https://doi.org/10.1117/12.366329>, 1999.
- 680 Calinski, T. and Harabasz, J.: A dendrite method for cluster analysis, *Comm. in Stats. - Theory & Methods*, 3, 1–27, <https://doi.org/10.1080/03610927408827101>, 1974.
- Chang, I., Gao, L., Adebisi, A. A., Doherty, S. J., Painemal, D., Smith, W. L., Lenhardt, E. D., Fakoya, A. A., Flynn, C. J., Zheng, J., Yang, Z., Castellanos, P., Da Silva, A. M., Zhang, Z., Wood, R., Zuidema, P., Christopher, S. A., and Redemann, J.: Regional aerosol warming enhanced by the diurnal cycle of low cloud, *Nat. Geosci.*, 18, 702–708, <https://doi.org/10.1038/s41561-025-01740-1>, 2025.
- 685 <https://doi.org/10.1038/s41561-025-01740-1>, 2025.
- Chau, K., Franklin, M., Lee, H., Garay, M., and Kalashnikova, O.: Temporal and Spatial Autocorrelation as Determinants of Regional AOD-PM_{2.5} Model Performance in the Middle East, *Remote Sensing*, 13, 3790, <https://doi.org/10.3390/rs13183790>, 2021.
- Chen, J., Liu, Y., Zhang, M., and Peng, Y.: Height Dependency of Aerosol-Cloud Interaction Regimes, *JGR Atmospheres*, 123, 491–506, <https://doi.org/10.1002/2017JD027431>, 2018.
- 690 <https://doi.org/10.1002/2017JD027431>, 2018.



- Chen, Y., Christensen, M. W., Diner, D. J., and Garay, M. J.: Aerosol-cloud interactions in ship tracks using Terra MODIS/MISR, *JGR Atmospheres*, 120, 2819–2833, <https://doi.org/10.1002/2014JD022736>, 2015.
- Choudhury, G. and Tesche, M.: Assessment of CALIOP-Derived CCN Concentrations by In Situ Surface Measurements, *Remote Sensing*, 14, 3342, <https://doi.org/10.3390/rs14143342>, 2022a.
- 695 Choudhury, G. and Tesche, M.: Estimating cloud condensation nuclei concentrations from CALIPSO lidar measurements, *Atmos. Meas. Tech.*, 15, 639–654, <https://doi.org/10.5194/amt-15-639-2022>, 2022b.
- Christensen, M. W., Neubauer, D., Poulsen, C. A., Thomas, G. E., McGarragh, G. R., Povey, A. C., Proud, S. R., and Grainger, R. G.: Unveiling aerosol–cloud interactions – Part 1: Cloud contamination in satellite products enhances the aerosol indirect forcing estimate, *Atmos. Chem. Phys.*, 17, 13151–13164, <https://doi.org/10.5194/acp-17-13151-2017>, 2017.
- 700 Costantino, L. and Bréon, F.-M.: Aerosol indirect effect on warm clouds over South-East Atlantic, from co-located MODIS and CALIPSO observations, *Atmos. Chem. Phys.*, 13, 69–88, <https://doi.org/10.5194/acp-13-69-2013>, 2013.
- D’Alessandro, J. J., McFarquhar, G. M., Stith, J. L., Diao, M., DeMott, P. J., McCluskey, C. S., Hill, T. C. J., Roberts, G. C., and Sanchez, K. J.: An Evaluation of Phase, Aerosol-Cloud Interactions and Microphysical Properties of Single- and Multi-Layer Clouds Over the Southern Ocean Using in Situ Observations From SOCRATES, *JGR Atmospheres*, 128, e2023JD038610, <https://doi.org/10.1029/2023JD038610>, 2023.
- 705 Dedrick, J. L., Pelayo, C. N., Russell, L. M., Lubin, D., Mülmenstädt, J., and Miller, M.: Competition response of cloud supersaturation explains diminished Twomey effect for smoky aerosol in the tropical Atlantic, *Proc. Natl. Acad. Sci. U.S.A.*, 122, e2412247122, <https://doi.org/10.1073/pnas.2412247122>, 2025.
- Di Bernardino, A., Iannarelli, A. M., Casadio, S., Pisacane, G., Mevi, G., and Cacciani, M.: Classification of synoptic and local-scale wind patterns using k-means clustering in a Tyrrhenian coastal area (Italy), *Meteorol Atmos Phys*, 134, 30, <https://doi.org/10.1007/s00703-022-00871-z>, 2022.
- 710 Diamond, M. S., Dobracki, A., Freitag, S., Small Griswold, J. D., Heikkilä, A., Howell, S. G., Kacarab, M. E., Podolske, J. R., Saide, P. E., and Wood, R.: Time-dependent entrainment of smoke presents an observational challenge for assessing aerosol–cloud interactions over the southeast Atlantic Ocean, *Atmos. Chem. Phys.*, 18, 14623–14636, <https://doi.org/10.5194/acp-18-14623-2018>, 2018.
- 715 Doherty, S. J., Saide, P. E., Zuidema, P., Shinozuka, Y., Ferrada, G. A., Gordon, H., Mallet, M., Meyer, K., Painemal, D., Howell, S. G., Freitag, S., Dobracki, A., Podolske, J. R., Burton, S. P., Ferrare, R. A., Howes, C., Nabat, P., Carmichael, G. R., Da Silva, A., Pistone, K., Chang, I., Gao, L., Wood, R., and Redemann, J.: Modeled and observed properties related to the direct aerosol radiative effect of biomass burning aerosol over the southeastern Atlantic, *Atmos. Chem. Phys.*, 22, 1–46, <https://doi.org/10.5194/acp-22-1-2022>, 2022.
- 720 Douglas, A. and L’Ecuyer, T.: Quantifying variations in shortwave aerosol–cloud–radiation interactions using local meteorology and cloud state constraints, *Atmos. Chem. Phys.*, 19, 6251–6268, <https://doi.org/10.5194/acp-19-6251-2019>, 2019.



- 725 Fan, J., Wang, Y., Rosenfeld, D., and Liu, X.: Review of Aerosol–Cloud Interactions: Mechanisms, Significance, and Challenges, *Journal of the Atmospheric Sciences*, 73, 4221–4252, <https://doi.org/10.1175/JAS-D-16-0037.1>, 2016.
- Forster, P., Storelvmo, T., Armour, K., Collins, W., Dufresne, J.-L., Frame, D., Lunt, D. J., Mauritsen, T., Palmer, M. D., Watanabe, M., Wild, M., and Zhang, H.: The Earth’s Energy Budget, Climate Feedbacks and Climate Sensitivity, in: *Climate Change 2021 – The Physical Science Basis*, edited by: Masson-Delmotte, V., Zhai, P., Pirani, A., Connors, S. L., Péan, C., Berger, S., Caud, N., Chen, Y., Goldfarb, L., Gomis, M. I., Huang, M., Leitzell, K., Lonnoy, E.,
730 Matthews, J. B. R., Maycock, T. K., Waterfield, T., Yelekçi, O., Yu, R., and Zhou, B., Cambridge University Press, 571–658, 2021.
- Franco, M. A., Morais, F. G., Rizzo, L. V., Palácios, R., Valiati, R., Teixeira, M., Machado, L. A. T., and Artaxo, P.: Aerosol optical depth and water vapor variability assessed through autocorrelation analysis, *Meteorol Atmos Phys*, 136, 15, <https://doi.org/10.1007/s00703-024-01011-5>, 2024.
- 735 Fu, D., Di Girolamo, L., Rauber, R. M., McFarquhar, G. M., Nesbitt, S. W., Loveridge, J., Hong, Y., Van Dierenhoven, B., Cairns, B., Alexandrov, M. D., Lawson, P., Woods, S., Tanelli, S., Schmidt, S., Hostetler, C., and Scarino, A. J.: An evaluation of the liquid cloud droplet effective radius derived from MODIS, airborne remote sensing, and in situ measurements from CAMP² Ex, *Atmos. Chem. Phys.*, 22, 8259–8285, <https://doi.org/10.5194/acp-22-8259-2022>, 2022.
- 740 Gao, L., Redemann, J., and Lenhardt, E.: Machine Learning Predicted CCN Concentration for ORACLES ACI Study, <https://doi.org/10.5281/ZENODO.18626083>, 2026.
- Global Modeling And Assimilation Office and Pawson, S.: MERRA-2 inst3_3d_asm_Np: 3d,3-Hourly,Instantaneous,Pressure-Level,Assimilation,Assimilated Meteorological Fields V5.12.4, <https://doi.org/10.5067/QBZ6MG944HW0>, 2015.
- 745 Goren, T. and Rosenfeld, D.: Satellite observations of ship emission induced transitions from broken to closed cell marine stratocumulus over large areas, *J. Geophys. Res.*, 117, 2012JD017981, <https://doi.org/10.1029/2012JD017981>, 2012.
- Gryspeerd, E. and Stier, P.: Regime-based analysis of aerosol-cloud interactions, *Geophysical Research Letters*, 39, 2012GL053221, <https://doi.org/10.1029/2012GL053221>, 2012.
- Gryspeerd, E., Stier, P., and Partridge, D. G.: Satellite observations of cloud regime development: the role of aerosol processes,
750 *Atmos. Chem. Phys.*, 14, 1141–1158, <https://doi.org/10.5194/acp-14-1141-2014>, 2014.
- Gryspeerd, E., Goren, T., Sourdeval, O., Quaas, J., Mülmenstädt, J., Dipu, S., Unglaub, C., Gettelman, A., and Christensen, M.: Constraining the aerosol influence on cloud liquid water path, *Atmos. Chem. Phys.*, 19, 5331–5347, <https://doi.org/10.5194/acp-19-5331-2019>, 2019.
- Gryspeerd, E., Glassmeier, F., Feingold, G., Hoffmann, F., and Murray-Watson, R. J.: Observing short-timescale cloud
755 development to constrain aerosol–cloud interactions, *Atmos. Chem. Phys.*, 22, 11727–11738, <https://doi.org/10.5194/acp-22-11727-2022>, 2022.



- 760 Gupta, S., McFarquhar, G. M., O'Brien, J. R., Delene, D. J., Poellot, M. R., Dobracki, A., Podolske, J. R., Redemann, J.,
LeBlanc, S. E., Segal-Rozenhaimer, M., and Pistone, K.: Impact of the variability in vertical separation between
biomass burning aerosols and marine stratocumulus on cloud microphysical properties over the Southeast Atlantic,
Atmos. Chem. Phys., 21, 4615–4635, <https://doi.org/10.5194/acp-21-4615-2021>, 2021.
- Gupta, S., McFarquhar, G. M., O'Brien, J. R., Poellot, M. R., Delene, D. J., Miller, R. M., and Small Griswold, J. D.: Factors
affecting precipitation formation and precipitation susceptibility of marine stratocumulus with variable above- and
below-cloud aerosol concentrations over the Southeast Atlantic, *Atmos. Chem. Phys.*, 22, 2769–2793,
<https://doi.org/10.5194/acp-22-2769-2022>, 2022a.
- 765 Gupta, S., McFarquhar, G. M., O'Brien, J. R., Poellot, M. R., Delene, D. J., Chang, I., Gao, L., Xu, F., and Redemann, J.: In
situ and satellite-based estimates of cloud properties and aerosol–cloud interactions over the southeast Atlantic Ocean,
Atmos. Chem. Phys., 22, 12923–12943, <https://doi.org/10.5194/acp-22-12923-2022>, 2022b.
- Hansen, J., Sato, M., and Ruedy, R.: Radiative forcing and climate response, *J. Geophys. Res.*, 102, 6831–6864,
<https://doi.org/10.1029/96JD03436>, 1997.
- 770 Heintzenberg, J., Birmili, W., Wiedensohler, A., Nowak, A., and Tuch, T.: Structure, variability and persistence of the
submicrometre marine aerosol, *Tellus B: Chemical and Physical Meteorology*, 56, 357,
<https://doi.org/10.3402/tellusb.v56i4.16450>, 2004.
- Hernández Pardo, L., Toledo Machado, L. A., Amore Cecchini, M., and Sánchez Gácita, M.: Quantifying the aerosol effect
on droplet size distribution at cloud top, *Atmos. Chem. Phys.*, 19, 7839–7857, [https://doi.org/10.5194/acp-19-7839-](https://doi.org/10.5194/acp-19-7839-2019)
775 [2019](https://doi.org/10.5194/acp-19-7839-2019), 2019.
- Jia, H., Ma, X., Quaas, J., Yin, Y., and Qiu, T.: Is positive correlation between cloud droplet effective radius and aerosol optical
depth over land due to retrieval artifacts or real physical processes?, *Atmos. Chem. Phys.*, 19, 8879–8896,
<https://doi.org/10.5194/acp-19-8879-2019>, 2019.
- Jose, S., Nair, V. S., and Babu, S. S.: Anthropogenic emissions from South Asia reverses the aerosol indirect effect over the
780 northern Indian Ocean, *Sci Rep*, 10, 18360, <https://doi.org/10.1038/s41598-020-74897-x>, 2020.
- Kacarab, M., Thornhill, K. L., Dobracki, A., Howell, S. G., O'Brien, J. R., Freitag, S., Poellot, M. R., Wood, R., Zuidema, P.,
Redemann, J., and Nenes, A.: Biomass burning aerosol as a modulator of the droplet number in the southeast Atlantic
region, *Atmos. Chem. Phys.*, 20, 3029–3040, <https://doi.org/10.5194/acp-20-3029-2020>, 2020.
- 785 Kaufman, Y. J., Haywood, J. M., Hobbs, P. V., Hart, W., Kleidman, R., and Schmid, B.: Remote sensing of vertical
distributions of smoke aerosol off the coast of Africa, *Geophys. Res. Lett.*, 30,
<https://doi.org/10.1029/2003GL017068>, 2003.
- Khatri, P., Hayasaka, T., Holben, B. N., Singh, R. P., Letu, H., and Tripathi, S. N.: Increased aerosols can reverse Twomey
effect in water clouds through radiative pathway, *Sci Rep*, 12, 20666, <https://doi.org/10.1038/s41598-022-25241-y>,
2022.



- 790 Kim, B., Miller, M. A., Schwartz, S. E., Liu, Y., and Min, Q.: The role of adiabaticity in the aerosol first indirect effect, *J. Geophys. Res.*, 113, 2007JD008961, <https://doi.org/10.1029/2007JD008961>, 2008.
- King, N. J., Bower, K. N., Crosier, J., and Crawford, I.: Evaluating MODIS cloud retrievals with in situ observations from VOCALS-REx, *Atmos. Chem. Phys.*, 13, 191–209, <https://doi.org/10.5194/acp-13-191-2013>, 2013.
- King, W. D., Parkin, D. A., and Handsworth, R. J.: A Hot-Wire Liquid Water Device Having Fully Calculable Response
795 Characteristics, *J. Appl. Meteor.*, 17, 1809–1813, [https://doi.org/10.1175/1520-0450\(1978\)017%253C1809:AHWLWD%253E2.0.CO;2](https://doi.org/10.1175/1520-0450(1978)017%253C1809:AHWLWD%253E2.0.CO;2), 1978.
- Klein, S. A. and Hartmann, D. L.: The Seasonal Cycle of Low Stratiform Clouds, *J. Climate*, 6, 1587–1606, [https://doi.org/10.1175/1520-0442\(1993\)006%253C1587:TSCOLS%253E2.0.CO;2](https://doi.org/10.1175/1520-0442(1993)006%253C1587:TSCOLS%253E2.0.CO;2), 1993.
- Koch, D. and Del Genio, A. D.: Black carbon semi-direct effects on cloud cover: review and synthesis, *Atmos. Chem. Phys.*,
800 10, 7685–7696, <https://doi.org/10.5194/acp-10-7685-2010>, 2010.
- Lance, S., Brock, C. A., Rogers, D., and Gordon, J. A.: Water droplet calibration of the Cloud Droplet Probe (CDP) and in-flight performance in liquid, ice and mixed-phase clouds during ARCPAC, *Atmos. Meas. Tech.*, 3, 1683–1706, <https://doi.org/10.5194/amt-3-1683-2010>, 2010.
- LeBlanc, S. E., Segal-Rozenhaimer, M., Redemann, J., Flynn, C., Johnson, R. R., Dunagan, S. E., Dahlgren, R., Kim, J., Choi,
805 M., Da Silva, A., Castellanos, P., Tan, Q., Ziemba, L., Lee Thornhill, K., and Kacenelenbogen, M.: Airborne observations during KORUS-AQ show that aerosol optical depths are more spatially self-consistent than aerosol intensive properties, *Atmos. Chem. Phys.*, 22, 11275–11304, <https://doi.org/10.5194/acp-22-11275-2022>, 2022.
- Lenhardt, E. D., Gao, L., Redemann, J., Xu, F., Burton, S. P., Cairns, B., Chang, I., Ferrare, R. A., Hostetler, C. A., Saide, P. E., Howes, C., Shinozuka, Y., Stamnes, S., Kacarab, M., Dobracki, A., Wong, J., Freitag, S., and Nenes, A.: Use of
810 lidar aerosol extinction and backscatter coefficients to estimate cloud condensation nuclei (CCN) concentrations in the southeast Atlantic, *Atmos. Meas. Tech.*, 16, 2037–2054, <https://doi.org/10.5194/amt-16-2037-2023>, 2023.
- Li, Z., Painemal, D., Feng, Y., and Zheng, X.: Progress in the quantification of aerosol-cloud interactions estimated from the CALIPSO-CloudSat-Aqua/MODIS record, <https://doi.org/10.5194/egusphere-2025-4769>, 6 October 2025.
- Lihavainen, H., Kerminen, V.-M., and Remer, L. A.: Aerosol-cloud interaction determined by both in situ and satellite data
815 over a northern high-latitude site, *Atmos. Chem. Phys.*, 10, 10987–10995, <https://doi.org/10.5194/acp-10-10987-2010>, 2010.
- Lohmann, U., Koren, I., and Kaufman, Y. J.: Disentangling the role of microphysical and dynamical effects in determining cloud properties over the Atlantic, *Geophysical Research Letters*, 33, 2005GL024625, <https://doi.org/10.1029/2005GL024625>, 2006.
- 820 Ma, X., Jia, H., Yu, F., and Quaas, J.: Opposite Aerosol Index-Cloud Droplet Effective Radius Correlations Over Major Industrial Regions and Their Adjacent Oceans, *Geophysical Research Letters*, 45, 5771–5778, <https://doi.org/10.1029/2018GL077562>, 2018.



- Malavelle, F. F., Haywood, J. M., Jones, A., Gettelman, A., Clarisse, L., Bauduin, S., Allan, R. P., Karset, I. H. H., Kristjánsson, J. E., Oreopoulos, L., Cho, N., Lee, D., Bellouin, N., Boucher, O., Grosvenor, D. P., Carslaw, K. S., Dhomse, S.,
825 Mann, G. W., Schmidt, A., Coe, H., Hartley, M. E., Dalvi, M., Hill, A. A., Johnson, B. T., Johnson, C. E., Knight, J. R., O'Connor, F. M., Partridge, D. G., Stier, P., Myhre, G., Platnick, S., Stephens, G. L., Takahashi, H., and Thordarson, T.: Strong constraints on aerosol–cloud interactions from volcanic eruptions, *Nature*, 546, 485–491, <https://doi.org/10.1038/nature22974>, 2017.
- Matsui, T., Masunaga, H., Kreidenweis, S. M., Pielke, R. A., Tao, W., Chin, M., and Kaufman, Y. J.: Satellite-based assessment
830 of marine low cloud variability associated with aerosol, atmospheric stability, and the diurnal cycle, *J. Geophys. Res.*, 111, 2005JD006097, <https://doi.org/10.1029/2005JD006097>, 2006.
- Mauger, G. S. and Norris, J. R.: Meteorological bias in satellite estimates of aerosol–cloud relationships, *Geophysical Research Letters*, 34, 2007GL029952, <https://doi.org/10.1029/2007GL029952>, 2007.
- McComiskey, A., Feingold, G., Frisch, A. S., Turner, D. D., Miller, M. A., Chiu, J. C., Min, Q., and Ogren, J. A.: An assessment
835 of aerosol–cloud interactions in marine stratus clouds based on surface remote sensing, *J. Geophys. Res.*, 114, 2008JD011006, <https://doi.org/10.1029/2008JD011006>, 2009.
- McCoy, D. T., Bender, F. A. -M., Mohrmann, J. K. C., Hartmann, D. L., Wood, R., and Grosvenor, D. P.: The global aerosol–cloud first indirect effect estimated using MODIS, MERRA, and AeroCom, *JGR Atmospheres*, 122, 1779–1796, <https://doi.org/10.1002/2016JD026141>, 2017.
- 840 McFarquhar, G. M.: A New Representation of Collision-Induced Breakup of Raindrops and Its Implications for the Shapes of Raindrop Size Distributions, *J. Atmos. Sci.*, 61, 777–794, [https://doi.org/10.1175/1520-0469\(2004\)061%253C0777:ANROCB%253E2.0.CO;2](https://doi.org/10.1175/1520-0469(2004)061%253C0777:ANROCB%253E2.0.CO;2), 2004.
- Mellado, J. P.: Cloud-Top Entrainment in Stratocumulus Clouds, *Annu. Rev. Fluid Mech.*, 49, 145–169, <https://doi.org/10.1146/annurev-fluid-010816-060231>, 2017.
- 845 Meyer, K., Platnick, S., Arnold, G. T., Amarasinghe, N., Miller, D., Small-Griswold, J., Witte, M., Cairns, B., Gupta, S., McFarquhar, G., and O'Brien, J.: Evaluating spectral cloud effective radius retrievals from the Enhanced MODIS Airborne Simulator (eMAS) during ORACLES, *Atmos. Meas. Tech.*, 18, 981–1011, <https://doi.org/10.5194/amt-18-981-2025>, 2025.
- Milligan, G. W. and Cooper, M. C.: A study of standardization of variables in cluster analysis, *Journal of Classification*, 5,
850 181–204, <https://doi.org/10.1007/BF01897163>, 1988.
- Min, Q., Joseph, E., Lin, Y., Min, L., Yin, B., Daum, P. H., Kleinman, L. I., Wang, J., and Lee, Y. -N.: Comparison of MODIS cloud microphysical properties with in-situ measurements over the Southeast Pacific, *Atmos. Chem. Phys.*, 12, 11261–11273, <https://doi.org/10.5194/acp-12-11261-2012>, 2012.
- 855 Modini, R. L., Frossard, A. A., Ahlm, L., Russell, L. M., Corrigan, C. E., Roberts, G. C., Hawkins, L. N., Schroder, J. C., Bertram, A. K., Zhao, R., Lee, A. K. Y., Abbatt, J. P. D., Lin, J., Nenes, A., Wang, Z., Wonauschütz, A., Sorooshian, A., Noone, K. J., Jonsson, H., Seinfeld, J. H., Toom-Sauntry, D., Macdonald, A. M., and Leaitch, W. R.: Primary



- marine aerosol-cloud interactions off the coast of California, *JGR Atmospheres*, 120, 4282–4303, <https://doi.org/10.1002/2014JD022963>, 2015.
- 860 Murray-Watson, R. J. and Gryspeerdt, E.: Stability-dependent increases in liquid water with droplet number in the Arctic, *Atmos. Chem. Phys.*, 22, 5743–5756, <https://doi.org/10.5194/acp-22-5743-2022>, 2022.
- Myhre, G., Stordal, F., Johnsrud, M., Kaufman, Y. J., Rosenfeld, D., Storelvmo, T., Kristjansson, J. E., Berntsen, T. K., Myhre, A., and Isaksen, I. S. A.: Aerosol-cloud interaction inferred from MODIS satellite data and global aerosol models, *Atmos. Chem. Phys.*, 7, 3081–3101, <https://doi.org/10.5194/acp-7-3081-2007>, 2007.
- 865 Nakajima, T. and King, M. D.: Determination of the Optical Thickness and Effective Particle Radius of Clouds from Reflected Solar Radiation Measurements. Part I: Theory, *J. Atmos. Sci.*, 47, 1878–1893, [https://doi.org/10.1175/1520-0469\(1990\)047%253C1878:DOTOTA%253E2.0.CO;2](https://doi.org/10.1175/1520-0469(1990)047%253C1878:DOTOTA%253E2.0.CO;2), 1990.
- Oh, D., Noh, Y., and Hoffmann, F.: Paths From Aerosol Particles to Activation and Cloud Droplets in Shallow Cumulus Clouds: The Roles of Entrainment and Supersaturation Fluctuations, *JGR Atmospheres*, 128, e2022JD038450, <https://doi.org/10.1029/2022JD038450>, 2023.
- 870 ORACLES Science Team: Suite of Aerosol, Cloud, and Related Data Acquired Aboard P3 During ORACLES 2016, Version 3, NASA Ames Earth Science Project Office (ESPO) [data set], https://doi.org/10.5067/Suborbital/ORACLES/P3/2016_V3, 2021a.
- ORACLES Science Team: Suite of Aerosol, Cloud, and Related Data Acquired Aboard ER2 During ORACLES 2016, Version 3, NASA Ames Earth Science Project Office (ESPO) [data set],
875 https://doi.org/10.5067/Suborbital/ORACLES/ER2/2016_V3, 2021b.
- ORACLES Science Team: Suite of Aerosol, Cloud, and Related Data Acquired Aboard P3 During ORACLES 2017, Version 3, NASA Ames Earth Science Project Office (ESPO) [data set],
https://doi.org/10.5067/Suborbital/ORACLES/P3/2017_V3, 2021c.
- ORACLES Science Team: Suite of Aerosol, Cloud, and Related Data Acquired Aboard P3 During ORACLES 2018, Version 3, NASA Ames Earth Science Project Office (ESPO) [data set],
880 https://doi.org/10.5067/Suborbital/ORACLES/P3/2018_V3, 2021d.
- Painemal, D. and Zuidema, P.: Microphysical variability in southeast Pacific Stratocumulus clouds: synoptic conditions and radiative response, *Atmos. Chem. Phys.*, 10, 6255–6269, <https://doi.org/10.5194/acp-10-6255-2010>, 2010.
- Painemal, D. and Zuidema, P.: Assessment of MODIS cloud effective radius and optical thickness retrievals over the Southeast Pacific with VOCALS-REx in situ measurements: MODIS VALIDATION DURING VOCALS-REx, *J. Geophys. Res.*, 116, n/a-n/a, <https://doi.org/10.1029/2011JD016155>, 2011.
- 885 Painemal, D., Chang, F.-L., Ferrare, R., Burton, S., Li, Z., Smith Jr., W. L., Minnis, P., Feng, Y., and Clayton, M.: Reducing uncertainties in satellite estimates of aerosol–cloud interactions over the subtropical ocean by integrating vertically resolved aerosol observations, *Atmos. Chem. Phys.*, 20, 7167–7177, <https://doi.org/10.5194/acp-20-7167-2020>,
890 2020.



- Painemal, D., Spangenberg, D., Smith Jr., W. L., Minnis, P., Cairns, B., Moore, R. H., Crosbie, E., Robinson, C., Thornhill, K. L., Winstead, E. L., and Ziemba, L.: Evaluation of satellite retrievals of liquid clouds from the GOES-13 imager and MODIS over the midlatitude North Atlantic during the NAAMES campaign, *Atmos. Meas. Tech.*, 14, 6633–6646, <https://doi.org/10.5194/amt-14-6633-2021>, 2021.
- 895 Painemal, D., Smith, W. L., Gupta, S., Moore, R., Cairns, B., McFarquhar, G. M., and O'Brien, J.: Can We Rely on Satellite Visible/Infrared Microphysical Retrievals of Boundary Layer Clouds in Partially Cloudy Scenes? Implications for Climate Research, *Geophysical Research Letters*, 52, e2024GL113825, <https://doi.org/10.1029/2024GL113825>, 2025.
- Pan, Z., Mao, F., Wang, W., Logan, T., and Hong, J.: Examining Intrinsic Aerosol-Cloud Interactions in South Asia Through Multiple Satellite Observations, *JGR Atmospheres*, 123, <https://doi.org/10.1029/2017JD028232>, 2018.
- 900 Perkins, R. J., Marinescu, P. J., Levin, E. J. T., Collins, D. R., and Kreidenweis, S. M.: Long- and short-term temporal variability in cloud condensation nuclei spectra over a wide supersaturation range in the Southern Great Plains site, *Atmos. Chem. Phys.*, 22, 6197–6215, <https://doi.org/10.5194/acp-22-6197-2022>, 2022.
- Rajapakshe, C., Zhang, Z., Yorks, J. E., Yu, H., Tan, Q., Meyer, K., Platnick, S., and Winker, D. M.: Seasonally transported aerosol layers over southeast Atlantic are closer to underlying clouds than previously reported, *Geophysical Research Letters*, 44, 5818–5825, <https://doi.org/10.1002/2017GL073559>, 2017.
- 905 Redemann, J. and Gao, L.: A machine learning paradigm for necessary observations to reduce uncertainties in aerosol climate forcing, *Nat Commun*, 15, 8343, <https://doi.org/10.1038/s41467-024-52747-y>, 2024.
- Redemann, J., Zhang, Q., Schmid, B., Russell, P. B., Livingston, J. M., Jonsson, H., and Remer, L. A.: Assessment of MODIS-derived visible and near-IR aerosol optical properties and their spatial variability in the presence of mineral dust, *Geophysical Research Letters*, 33, 2006GL026626, <https://doi.org/10.1029/2006GL026626>, 2006.
- 910 Redemann, J., Wood, R., Zuidema, P., Doherty, S. J., Luna, B., LeBlanc, S. E., Diamond, M. S., Shinozuka, Y., Chang, I. Y., Ueyama, R., Pfister, L., Ryoo, J.-M., Dobracki, A. N., da Silva, A. M., Longo, K. M., Kacenelenbogen, M. S., Flynn, C. J., Pistone, K., Knox, N. M., Piketh, S. J., Haywood, J. M., Formenti, P., Mallet, M., Stier, P., Ackerman, A. S., Bauer, S. E., Fridlind, A. M., Carmichael, G. R., Saide, P. E., Ferrada, G. A., Howell, S. G., Freitag, S., Cairns, B., Holben, B. N., Knobelspiesse, K. D., Tanelli, S., L'Ecuyer, T. S., Dzambo, A. M., Sy, O. O., McFarquhar, G. M., Poellot, M. R., Gupta, S., O'Brien, J. R., Nenes, A., Kacarab, M., Wong, J. P. S., Small-Griswold, J. D., Thornhill, K. L., Noone, D., Podolske, J. R., Schmidt, K. S., Pilewskie, P., Chen, H., Cochrane, S. P., Sedlacek, A. J., Lang, T. J., Stith, E., Segal-Rozenhaimer, M., Ferrare, R. A., Burton, S. P., Hostetler, C. A., Diner, D. J., Seidel, F. C., Platnick, S. E., Myers, J. S., Meyer, K. G., Spangenberg, D. A., Maring, H., and Gao, L.: An overview of the ORACLES (ObseRvations of Aerosols above CLouds and their intEractionS) project: aerosol–cloud–radiation interactions in the southeast Atlantic basin, *Atmos. Chem. Phys.*, 21, 1507–1563, <https://doi.org/10.5194/acp-21-1507-2021>, 2021.
- 920 Roberts, G. C. and Nenes, A.: A Continuous-Flow Streamwise Thermal-Gradient CCN Chamber for Atmospheric Measurements, *Aerosol Science and Technology*, 39, 206–221, <https://doi.org/10.1080/027868290913988>, 2005.



- 925 Roebeling, R. A., Placidi, S., Donovan, D. P., Russchenberg, H. W. J., and Feijt, A. J.: Validation of liquid cloud property retrievals from SEVIRI using ground-based observations, *Geophysical Research Letters*, 35, 2007GL032115, <https://doi.org/10.1029/2007GL032115>, 2008.
- Rose, D., Gunthe, S. S., Mikhailov, E., Frank, G. P., Dusek, U., Andreae, M. O., and Pöschl, U.: Calibration and measurement uncertainties of a continuous-flow cloud condensation nuclei counter (DMT-CCNC): CCN activation of ammonium sulfate and sodium chloride aerosol particles in theory and experiment, *Atmos. Chem. Phys.*, 8, 1153–1179, 930 <https://doi.org/10.5194/acp-8-1153-2008>, 2008.
- Rosenfeld, D.: Aerosol-Cloud Interactions Control of Earth Radiation and Latent Heat Release Budgets, *Space Sci Rev*, 125, 149–157, <https://doi.org/10.1007/s11214-006-9053-6>, 2006.
- Rosenfeld, D., Andreae, M. O., Asmi, A., Chin, M., De Leeuw, G., Donovan, D. P., Kahn, R., Kinne, S., Kivekäs, N., Kulmala, 935 M., Lau, W., Schmidt, K. S., Suni, T., Wagner, T., Wild, M., and Quaas, J.: Global observations of aerosol-cloud-precipitation-climate interactions: Aerosol-cloud-climate interactions, *Rev. Geophys.*, 52, 750–808, <https://doi.org/10.1002/2013RG000441>, 2014.
- Ross, K. E., Piketh, S. J., Bruintjes, R. T., Burger, R. P., Swap, R. J., and Annegarn, H. J.: Spatial and seasonal variations in CCN distribution and the aerosol-CCN relationship over southern Africa: CCN DISTRIBUTION AND THE 940 AEROSOL-CCN RELATIONSHIP, *J. Geophys. Res.*, 108, n/a-n/a, <https://doi.org/10.1029/2002JD002384>, 2003.
- Ryoo, J.-M., Pfister, L., Ueyama, R., Zuidema, P., Wood, R., Chang, I., and Redemann, J.: A meteorological overview of the ORACLES (ObseRVations of Aerosols above CLouds and their intERactionS) campaign over the southeastern Atlantic during 2016–2018: Part 1 – Climatology, *Atmos. Chem. Phys.*, 21, 16689–16707, <https://doi.org/10.5194/acp-21-16689-2021>, 2021.
- 945 Seinfeld, J. H., Bretherton, C., Carslaw, K. S., Coe, H., DeMott, P. J., Dunlea, E. J., Feingold, G., Ghan, S., Guenther, A. B., Kahn, R., Kraucunas, I., Kreidenweis, S. M., Molina, M. J., Nenes, A., Penner, J. E., Prather, K. A., Ramanathan, V., Ramaswamy, V., Rasch, P. J., Ravishankara, A. R., Rosenfeld, D., Stephens, G., and Wood, R.: Improving our fundamental understanding of the role of aerosol–cloud interactions in the climate system, *Proc. Natl. Acad. Sci. U.S.A.*, 113, 5781–5790, <https://doi.org/10.1073/pnas.1514043113>, 2016.
- 950 Shinozuka, Y. and Redemann, J.: Horizontal variability of aerosol optical depth observed during the ARCTAS airborne experiment, *Atmos. Chem. Phys.*, 11, 8489–8495, <https://doi.org/10.5194/acp-11-8489-2011>, 2011.
- Shinozuka, Y., Clarke, A. D., Nenes, A., Jefferson, A., Wood, R., McNaughton, C. S., Ström, J., Tunved, P., Redemann, J., Thornhill, K. L., Moore, R. H., Latham, T. L., Lin, J. J., and Yoon, Y. J.: The relationship between cloud condensation nuclei (CCN) concentration and light extinction of dried particles: indications of underlying aerosol processes and 955 implications for satellite-based CCN estimates, *Atmos. Chem. Phys.*, 15, 7585–7604, <https://doi.org/10.5194/acp-15-7585-2015>, 2015.



- Sorooshian, A., Feingold, G., Lebsock, M. D., Jiang, H., and Stephens, G. L.: On the precipitation susceptibility of clouds to aerosol perturbations, *Geophysical Research Letters*, 36, 2009GL038993, <https://doi.org/10.1029/2009GL038993>, 2009.
- 960 Sterzinger, L. J. and Igel, A. L.: Above-cloud concentrations of cloud condensation nuclei help to sustain some Arctic low-level clouds, *Atmos. Chem. Phys.*, 24, 3529–3540, <https://doi.org/10.5194/acp-24-3529-2024>, 2024.
- Stevens, B. and Feingold, G.: Untangling aerosol effects on clouds and precipitation in a buffered system, *Nature*, 461, 607–613, <https://doi.org/10.1038/nature08281>, 2009.
- Stier, P.: Limitations of passive remote sensing to constrain global cloud condensation nuclei, *Atmos. Chem. Phys.*, 16, 6595–6607, <https://doi.org/10.5194/acp-16-6595-2016>, 2016.
- 965 Sun, J., Leighton, H., Yau, M. K., and Ariya, P.: Numerical evidence for cloud droplet nucleation at the cloud-environment interface, *Atmos. Chem. Phys.*, 12, 12155–12164, <https://doi.org/10.5194/acp-12-12155-2012>, 2012.
- Tang, J., Wang, P., Mickley, L. J., Xia, X., Liao, H., Yue, X., Sun, L., and Xia, J.: Positive relationship between liquid cloud droplet effective radius and aerosol optical depth over Eastern China from satellite data, *Atmospheric Environment*, 84, 244–253, <https://doi.org/10.1016/j.atmosenv.2013.08.024>, 2014.
- 970 Twohy, C. H., Petters, M. D., Snider, J. R., Stevens, B., Tahnk, W., Wetzel, M., Russell, L., and Burnet, F.: Evaluation of the aerosol indirect effect in marine stratocumulus clouds: Droplet number, size, liquid water path, and radiative impact, *J. Geophys. Res.*, 110, 2004JD005116, <https://doi.org/10.1029/2004JD005116>, 2005.
- Twomey, S.: Pollution and the planetary albedo, *Atmospheric Environment* (1967), 8, 1251–1256, [https://doi.org/10.1016/0004-6981\(74\)90004-3](https://doi.org/10.1016/0004-6981(74)90004-3), 1974.
- 975 Várnai, T. and Marshak, A.: Analysis of co-located MODIS and CALIPSO observations near clouds, *Atmos. Meas. Tech.*, 5, 389–396, <https://doi.org/10.5194/amt-5-389-2012>, 2012.
- Wang, D., Yang, C. A., and Diao, M.: Validation of Satellite-Based Cloud Phase Distributions Using Global-Scale In Situ Airborne Observations, *Earth and Space Science*, 11, e2023EA003355, <https://doi.org/10.1029/2023EA003355>, 2024.
- 980 Warren, S., Hahn, C., London, J., Chervin, R., and Jenne, R.: Global Distribution of Total Cloud Cover and Cloud Type Amounts Over the Ocean, NSF National Center for Atmospheric Research, <https://doi.org/10.5065/D6QC01D1>, 1988.
- Wehr, T., Kubota, T., Tzeremes, G., Wallace, K., Nakatsuka, H., Ohno, Y., Koopman, R., Rusli, S., Kikuchi, M., Eisinger, M., Tanaka, T., Taga, M., Deghaye, P., Tomita, E., and Bernaerts, D.: The EarthCARE mission – science and system overview, *Atmos. Meas. Tech.*, 16, 3581–3608, <https://doi.org/10.5194/amt-16-3581-2023>, 2023.
- 985 Wood, R.: Stratocumulus Clouds, *Monthly Weather Review*, 140, 2373–2423, <https://doi.org/10.1175/MWR-D-11-00121.1>, 2012.



- 990 Wood, R.: Relationships between optical depth, liquid water path, droplet concentration, and effective radius in adiabatic layer
cloud, University of Washington, https://atmos.uw.edu/~robwood/papers/chilean_plume/optical_depth_relations.pdf, Accessed 20 Jan 2026, 2006.
- Wood, R. and Bretherton, C. S.: On the Relationship between Stratiform Low Cloud Cover and Lower-Tropospheric Stability, *Journal of Climate*, 19, 6425–6432, <https://doi.org/10.1175/JCLI3988.1>, 2006.
- 995 Zhang, S., Wang, M., Ghan, S. J., Ding, A., Wang, H., Zhang, K., Neubauer, D., Lohmann, U., Ferrachat, S., Takeamura, T.,
Gettelman, A., Morrison, H., Lee, Y., Shindell, D. T., Partridge, D. G., Stier, P., Kipling, Z., and Fu, C.: On the
characteristics of aerosol indirect effect based on dynamic regimes in global climate models, *Atmos. Chem. Phys.*,
16, 2765–2783, <https://doi.org/10.5194/acp-16-2765-2016>, 2016.
- Zhao, J., Ma, X., Quaas, J., and Yang, T.: How meteorological conditions influence aerosol-cloud interactions under different
pollution regimes, *Atmos. Chem. Phys.*, 25, 17701–17723, <https://doi.org/10.5194/acp-25-17701-2025>, 2025.
- 1000 Zheng, X., Dong, X., Xi, B., Logan, T., and Wang, Y.: Distinctive aerosol–cloud–precipitation interactions in marine boundary
layer clouds from the ACE-ENA and SOCRATES aircraft field campaigns, *Atmos. Chem. Phys.*, 24, 10323–10347,
<https://doi.org/10.5194/acp-24-10323-2024>, 2024.
- Zuidema, P., Redemann, J., Haywood, J., Wood, R., Piketh, S., Hipondoka, M., and Formenti, P.: Smoke and Clouds above
the Southeast Atlantic: Upcoming Field Campaigns Probe Absorbing Aerosol’s Impact on Climate, *Bulletin of the*
1005 *American Meteorological Society*, 97, 1131–1135, <https://doi.org/10.1175/BAMS-D-15-00082.1>, 2016.